Direct numerical simulations of two-dimensional chaotic natural convection in a differentially heated cavity of aspect ratio 4

By SHIHE XIN AND PATRICK LE QUÉRÉ

LIMSI-CNRS, BP 133, 91403-Orsay Cedex, France

Chaotic natural convection in a differentially heated air-filled cavity of aspect ratio 4 with adiabatic horizontal walls is investigated by direct numerical integration of the unsteady two-dimensional equations. Time integration is performed with a spectral algorithm using Chebyshev spatial approximations and a second-order finite-difference time-stepping scheme. Asymptotic solutions have been obtained for three values of the Rayleigh number based on cavity height up to 10^{10}. The time-averaged flow fields show that the flow structure increasingly departs from the well-known laminar one. Large recirculating zones located on the outer edge of the boundary layers form and move upstream with increasing Rayleigh number. The time-dependent solution is made up of travelling waves which run downstream in the boundary layers. The amplitude of these waves grows as they travel downstream and hook-like temperature patterns form at the outer edge of the thermal boundary layer. At the largest Rayleigh number investigated they grow to such a point that they result in the formation of large unsteady eddies that totally disrupt the boundary layers. These eddies throw hot and cold fluid into the upper and lower parts of the core region, resulting in thermally more homogeneous top and bottom regions that squeeze a region of increased stratification near the mid-cavity height. It is also shown that these large unsteady eddies keep the internal waves in the stratified core region excited. These simulations also give access to the second-order statistics such as turbulent kinetic energy, thermal and viscous dissipation, Reynolds stresses and turbulent heat fluxes.

1. Introduction

Natural convection is a recurrent phenomenon in the world around us and most of these natural convection flows, especially those encountered in engineering applications, are turbulent. Unsteady and turbulent natural convection has thus attracted increasing interest over the last decade for two main reasons: on the one hand there is a desire to improve our phenomenological understanding of turbulent natural convection and on the other hand there is a pressing need for numerical models capable of predicting the corresponding flow structures and related heat transfer in industrial applications.

Natural convection flows in enclosures are usually subdivided into two main classes, those heated from below and those heated from the side. The prototype configuration of the latter class is the differentially heated cavity. This configuration models many engineering applications such as cooling of electronic components, nuclear reactor insulation, ventilation of rooms. It is thus of considerable practical as well as

theoretical importance and has therefore become a classical problem in the convective heat transfer and fluid mechanics literature. Its two-dimensional modelization, also known by the name of a thermally driven cavity, was popularized by the workshop organized by de Vahl Davis & Jones (1980), and has also become one of the favourite problems for the testing of numerical methods for the resolution of incompressible recirculating flows of viscous fluid. In the past years most studies relevant to natural convection in cavities have focused on laminar steady and transient flow regimes (de Vahl Davis & Jones 1983; Haldenwang 1984; Ivey 1984; Patterson & Imberger 1980; Le Quéré 1991; Patterson & Armfield, 1990), the transition to unsteadiness and the *route to chaos* (Le Quéré 1987; Le Quéré & Penot 1987; Paolucci & Chenoweth 1989; Henkes 1990; Penot, Ndame & Le Quéré 1990; Ndame 1992). The corresponding conclusions are the following: for small values of the Rayleigh number laminar steady natural convection is observed, which, if the cavity aspect ratio is small enough, encompasses two sub-regimes, the conduction and the separated boundary layer regimes. When the Rayleigh number is increased above a critical value, unsteady convection is observed, due to the loss of stability of steady solutions. In air-filled cavities of aspect ratios smaller than or equal to 3, two distinct instability mechanisms have been found to be responsible for the onset of unsteadiness depending on the thermal boundary conditions imposed on the horizontal walls. On the other hand for aspect ratio larger than or equal to 4 the onset of unsteadiness is due to the instability of vertical boundary layers independently of the boundary conditions imposed on the horizontal walls. The onset of unsteadiness proceeds through a bifurcation which is of Hopf supercritical type. Subsequent investigations have shown that the route of transition to chaos seems to proceed through quasi-periodicity and intermittency (see Le Quéré 1994b for a review).

In contrast to the Rayleigh–Bénard configuration in which flows become turbulent at relatively low Rayleigh numbers and for which direct simulations have long been performed (see Lipps 1976 and Grötzbach 1982 amongst others), there have been only a few numerical studies of fully chaotic flows in differentially heated cavities. After the pioneering work of Fromm (1971), who demonstrated the feasibility of direct simulation, the first extensive study seems to be that of Paolucci (1990) who used a numerical algorithm in primitive variable formulation and an explicit first-order time-stepping code with second-order spatial differencing on a non-uniform grid. He performed a numerical simulation of two-dimensional turbulent natural convection in a square cavity with adiabatic horizontal walls for a Rayleigh number equal to 10^{10}. It is noted that the simulation was started from isothermal and quiescent conditions. In addition to providing detailed information on the structure of turbulent boundary layers and turbulent statistics, he found that the stratification in the core seems to achieve a constant dimensionless value of about 0.38.

We have similarly investigated fully chaotic natural convection in a differentially heated air-filled cavity of aspect ratio 4 with adiabatic horizontal walls using direct numerical integration of the two-dimensional unsteady Navier–Stokes equations. The two-dimensional unsteady equations written in primitive variables formulation under the Boussinesq approximation are integrated by a pseudo-spectral code, which has been extensively used to investigate transition to unsteadiness and to chaos. This algorithm combines spatial expansions in series of Chebyshev polynomials with a second-order finite-difference time-stepping scheme. The incompressibility condition is ensured by an influence matrix technique. Direct simulations of fully chaotic two-dimensional flows were performed for values of the Rayleigh number based on cavity height up to 10^{10} (two orders of magnitude above the critical value corresponding

to the onset of unsteadiness), that correspond to weakly turbulent flows in actual configurations.

We chose to perform these simulations in a cavity of aspect ratio 4 for the following reasons: the transition to unsteadiness and the route of chaos have been studied in detail in this particular configuration and it was therefore natural for us to continue with the same aspect ratio; secondly, what happens in a cavity whose sidewalls are maintained at constant uniform temperatures is to a large extent determined by the Rayleigh number based on cavity height and, consequently, considering a cavity of aspect ratio 4 thus allows us to use a small number of Chebyshev polynomials in the horizontal direction (by comparison with what would have been needed in a square cavity), which is numerically very interesting. These simulations have nonetheless required very large spatial resolutions: for a Rayleigh number of 10^{10}, for example, it was found necessary to use a 96×768 spatial resolution in the horizontal and vertical directions respectively. The increase in horizontal direction arises from the fact that as the Rayleigh number increases, the boundary layer thickness, which scales like $Ra^{-1/4}$ in the laminar regime, becomes exceedingly small, but since the Gauss–Lobatto grid is also very dense near the end points, the number of modes needed to maintain a prescribed accuracy scales roughly like $Ra^{1/8}$. The more dramatic increase in the vertical direction is due to the fact that, for increasing Rayleigh number, the transition point in the vertical boundary layer moves upstream (its relative location in the cavity) and small structures are generated around the mid-cavity height in a region where the number of Chebyshev modes needed to capture spatial scales of order ϵ scales like ϵ^{-1}.

The objectives of these simulations are twofold: to improve our understanding of the dynamics of chaotic convection in a differentially heated cavity on the one hand, but also to compute the statistical quantities (time-averaged fields, kinetic energy of the fluctuating velocity field, viscous and thermal dissipation rates, Reynolds stresses, turbulent heat fluxes, etc.) which are needed in conventional approaches to turbulence on the other hand. Although direct simulations of the unsteady laminar equations, which are at the present time restricted to simple geometries and academic configurations, or more likely large eddy simulations could ultimately become of general use in industrial applications, it seems clear that the computations of turbulent convection for engineering applications will still for a long time be achieved through numerical solution of Reynolds-averaged equations closed with appropriate turbulence models. Over the last few years turbulence models of increasing complexity have been used for turbulent natural convection flows in cavities (Fraikin, Portier & Fraikin 1980; Markatos & Pericleous 1984; Ozoe *et al.* 1986; To & Humphrey 1986; Giel & Schmidt 1990; Abrous & Emery 1989; Henkes 1990; Nobile, Sousa & Barozzi 1990; Le Breton 1991; Ince, Betts & Launder 1992). Accurate predictions of turbulent flows in various configurations seem hopeless in the framework of k-ϵ models even with low Reynolds number corrections and require second-moment closure models, which involve modelling of many terms (see Hanjalic 1994). In order to critically assess the validity of these models, to help understand their shortcomings and possibly improve them, it is necessary to obtain data on the flow structure and on the turbulence quantities that are used in the models, such as turbulence kinetic energy, viscous dissipation, Reynolds stresses or turbulent heat fluxes. In view of the difficulty in obtaining data from laboratory experiments in configurations with idealized boundary conditions such as those usually considered in numerical computations but rarely met in practice (Mergui, Penot & Tuhault 1992) and since the flow is very sensitive to these boundary conditions as highlighted by

Allard (1992), direct simulations can help provide these data. It is one of our goals to contribute to providing these data that will be needed for useful comparisons with solutions obtained from classical turbulence modelling approaches. As final introductory remarks, let us mention that we are fully aware that two-dimensional simulations, no matter how chaotic they might be, cannot reproduce real turbulent flows. It is however expected that, in this mildly turbulent regime, two-dimensional simulations can reproduce well the dynamics of the large-scale structures of the flow.

This paper is organized as follows: in the following section, we recall briefly the governing equations of the physical problem considered and the numerical algorithm used which has already been presented in detail by Le Quéré (1987, 1991). In §3 we present results of the direct numerical simulations, concerning the structure of the time-averaged flow field, its dynamics, some second-order statistics and results for the heat transfer. Some conclusions will be drawn in §4.

2. Governing equations and numerical algorithm

2.1. *Governing equations*

We consider a cavity of height H and width W (aspect ratio $A = H/W$) filled with a Newtonian viscous fluid of thermal diffusivity α and kinematic viscosity v. It is submitted to a temperature difference ΔT $(= T_h - T_c > 0)$ at the vertical walls (constant uniform temperatures T_h and T_c are imposed) while the top and bottom walls are adiabatic. We assume that the flow in the cavity is governed by the two-dimensional unsteady Boussinesq equations.

These equations are made dimensionless with the following reference quantities: $L_r = H$ for length, $V_r = (\alpha/H)Ra^{0.5}$ for velocity and $t_r = (H^2/\alpha)Ra^{-0.5}$ for time where Ra is the Rayleigh number $(g\beta\Delta TH^3)/(v\alpha)$. It is noted that the above reference quantities result in vertical velocity components of order 1. With this set of reference quantities and the scaled temperature Θ defined as $(T - T_r)/(T_h - T_c)$ with $T_r = (T_h + T_c)/2$, the governing unsteady Boussinesq equations in primitive variables read

$$\left.\begin{array}{c} \dfrac{\partial u}{\partial x} + \dfrac{\partial w}{\partial z} = 0, \\[2mm] \dfrac{\partial u}{\partial t} + u\dfrac{\partial u}{\partial x} + w\dfrac{\partial u}{\partial z} = -\dfrac{\partial P}{\partial x} + \dfrac{Pr}{Ra^{0.5}}\left(\dfrac{\partial^2 u}{\partial x^2} + \dfrac{\partial^2 u}{\partial z^2}\right), \\[2mm] \dfrac{\partial w}{\partial t} + u\dfrac{\partial w}{\partial x} + w\dfrac{\partial w}{\partial z} = -\dfrac{\partial P}{\partial z} + \dfrac{Pr}{Ra^{0.5}}\left(\dfrac{\partial^2 w}{\partial x^2} + \dfrac{\partial^2 w}{\partial z^2}\right) + Pr\,\Theta, \\[2mm] \dfrac{\partial \Theta}{\partial t} + u\dfrac{\partial \Theta}{\partial x} + w\dfrac{\partial \Theta}{\partial z} = \dfrac{1}{Ra^{0.5}}\left(\dfrac{\partial^2 \Theta}{\partial x^2} + \dfrac{\partial^2 \Theta}{\partial z^2}\right), \end{array}\right\} \quad (2.1)$$

where u and w are the horizontal and vertical velocity components respectively, Pr is Prandtl number $(= v/\alpha)$ and P is the pressure deviation from the hydrostatic pressure made dimensionless with the mean density multiplied by V_r^2. The problem (2.1) is then defined on the computational domain that extends from 0 to $1/A$ in the x-direction and from 0 to 1 in the z-direction. The boundary conditions are

   u and $w = 0$ on all four walls,
   $\Theta = 0.5$ on $x = 0$ and $\Theta = -0.5$ on $x = 1/A$, $0 \leqslant z \leqslant 1$,
   $\partial\Theta/\partial z = 0$ on $z = 0$ and 1, $0 \leqslant x \leqslant 1/A$.
In dimensionless form the configuration depends on three parameters: the Prandtl

number, the cavity aspect ratio and the Rayleigh number. If we furthermore consider that the cavity is filled with air corresponding to a Prandtl number of 0.71 and that its aspect ratio is equal to 4, the configuration at hand then solely depends on the Rayleigh number.

2.2. *Numerical algorithm*

The two-dimensional unsteady Boussinesq equations are then integrated in velocity–pressure formulation by a pseudo-spectral algorithm combining spatial expansion in series of Chebyshev polynomials with a semi-implicit second-order finite-difference time-stepping scheme.

2.2.1. *Spatial discretization*

Spatial discretization is based on the use of tensor products of Chebyshev polynomials $T_i(2Ax-1) \times T_j(2z-1)$ as basis expansion functions; $f(x, z, t)$, a two-dimensional field representing one of the four dependent variables u, w, P and Θ, is then expressed in a double truncated series as follows:

$$f(x, z, t) = \sum_{i=0}^{N} \sum_{j=0}^{M} f_{ij}(t) \times T_i(2Ax - 1) \times T_j(2z - 1)$$

where $T_i(x) = \cos(i \arccos(x))$. The spectral coefficients f_{ij} are obtained by using the discrete orthogonality relationship:

$$f_{ij}(t) = \frac{4}{\bar{c}_i N \bar{c}_j M} \sum_{l=0}^{N} \sum_{m=0}^{M} \frac{1}{\bar{c}_l \bar{c}_m} \times f(x_l, z_m, t) \times T_i(2Ax_l - 1) \times T_j(2z_m - 1)$$

where x_l and z_m are the Gauss–Lobatto points, $\{ x_l = (1 - \cos(\pi l/N))/(2A), l = 0, \ldots, N \}$ and $\{ z_m = (1 - \cos(\pi m/M))/2, m = 0, \ldots, M \}$; $\bar{c}_0 = \bar{c}_N = 2, \bar{c}_i = 1, 0 < i < N$.

2.2.2. *Time discretization*

The time discretization scheme used is classically of finite-difference type. We note that the use of Chebyshev polynomials as basis functions requires an implicit or semi-implicit treatment of the viscous or diffusion terms and while the nonlinear terms are generally discretized explicitly. Here the time-stepping scheme combines a second-order backward Euler scheme for the diffusion terms with an explicit second-order Adams–Bashforth extrapolation for the nonlinear terms (Vanel, Peyret & Bontoux 1986). When applied to a scalar advection-diffusion equation such as

$$\frac{\partial f}{\partial t} + V \cdot \nabla f = \nabla^2 f$$

this scheme reads

$$\frac{3f^{n+1} - 4f^n + f^{n-1}}{2\Delta t} + 2(V \cdot \nabla f)^n - (V \cdot \nabla f)^{n-1} = \nabla^2 f^{n+1}$$

which can be cast in a Helmholtz equation for the unknown f^{n+1}:

$$\nabla^2 f^{n+1} - \lambda f^{n+1} = S_f$$

where $\lambda = 3/(2\Delta t)$. The source term S_f of this equation is made up of all the known quantities at the previous time levels $n\Delta t$ and $(n-1)\Delta t$. The nonlinear term $V \cdot \nabla f$ is classically calculated in physical space at the Gauss–Lobatto points and then transformed into spectral space, since the resulting Helmholtz equation is solved

in spectral space using the tau-method and the partial diagonalization technique proposed by Haidvogel & Zang (1979).

2.2.3. Incompressibility

When the above time-stepping scheme is applied to problem (2.1), the resulting equations read

$$
\left.
\begin{aligned}
\frac{\partial u^{n+1}}{\partial x} + \frac{\partial w^{n+1}}{\partial z} &= 0, \\
\frac{Pr}{Ra^{0.5}} \nabla^2 u^{n+1} - \lambda u^{n+1} &= S_u + \frac{\partial P}{\partial x}, \\
\frac{Pr}{Ra^{0.5}} \nabla^2 w^{n+1} - \lambda w^{n+1} &= S_w + \frac{\partial P}{\partial z}, \\
\frac{1}{Ra^{0.5}} \nabla^2 \Theta^{n+1} - \lambda \Theta^{n+1} &= S_\Theta,
\end{aligned}
\right\}
\tag{2.2}
$$

where S_u, S_w and S_Θ are given respectively by

$$
S_f = \frac{-4f^n + f^{n-1}}{2\Delta t} + 2(\boldsymbol{V} \cdot \nabla f)^n - (\boldsymbol{V} \cdot \nabla f)^{n-1} - C_f Pr \Theta
$$

with $C_u = C_\Theta = 0$ and $C_w = 1$.

The first three equations of (2.2) constitute an unsteady Stokes problem that has to be solved at every time step. By taking the divergence of the two momentum equations of the Stokes problem we get

$$
(Pr/Ra^{0.5}) \nabla^2 D^{n+1} - \lambda D^{n+1} = \frac{\partial S_u}{\partial x} + \frac{\partial S_w}{\partial z} + \nabla^2 P
$$

where $D = \partial u/\partial x + \partial w/\partial z$. Assuming the flow is divergence free at $n+1$ yields the classical Poisson equation for pressure:

$$
\nabla^2 P = -\left(\frac{\partial S_u}{\partial x} + \frac{\partial S_w}{\partial z} \right).
$$

It is clear that when this Poisson equation for the pressure field holds the flow divergence verifies $(Pr/Ra^{0.5}) \nabla^2 D^{n+1} - \lambda D^{n+1} = 0$ and the flow is divergence free if and only if $D^{n+1} = 0$ at the boundary of the computational domain, i.e. on the cavity walls. The essence of the influence or capacitance matrix technique is to supplement the Poisson equation for pressure with Dirichlet boundary conditions that warrant $D^{n+1} = 0$ on the cavity walls. These Dirichlet boundary conditions for pressure can be determined efficiently in one iteration only since the relationship between the pressure on the cavity walls and the divergence is linear. This influence matrix technique was proposed by Kleiser & Schumann (1980) for the one-dimensional Chebyshev problem and extended to a two-dimensional Chebyshev configuration by Le Quéré & Alziary de Roquefort (1982, 1985). Note however that, due to the non-commutativity of the discrete divergence and tau-projection operators (see Haldenwang 1986), the velocity field is not divergence free in the interior of the computational domain. Recently, Tuckerman (1989) proposed a complete divergence-free method based on the use of the Shermann–Morrison–Woodbury formula. The computations reported below were performed with the initial version of the algorithm but the residual error was kept small enough to ensure very accurate solutions.

3. Results

The presentation of the results will be done in five subsections: we first discuss the numerical characteristics of the time integrations; we then present the time-averaged flow structures, the flow dynamics, some 'turbulent' statistics and heat transfer coefficients in the second, third, forth and fifth subsections, respectively.

3.1. *Numerical requirements*

Over the past few years the appearance of unsteadiness and the transition to chaos of flows in an air-filled cavity of aspect ratio 4 have been numerically and experimentally studied in detail (Le Quéré 1987; Le Quéré & Penot 1987; Penot *et al.* 1990; Ndame 1992). It was shown that the flow in the cavity undergoes a supercritical Hopf bifurcation at a Rayleigh number based on cavity height of 1.03×10^8. For small supercritical values the flow is periodic in time and the unsteadiness is due to an absolute instability of the vertical boundary layers. (Note that this absolute instability occurs long after the vertical boundary layers have become convectively unstable.) Chaotic behaviour is first observed at a Rayleigh number of 2.3×10^8, which shows that the transition to chaos takes place over a relatively small range of Rayleigh number. This chaos is however only temporal chaos that is present in the time traces of temperature or velocity signals but cannot be distinguished in the spatial structure of the flow which is still very well organized.

In order to approach chaotic flows which exhibit randomness in space as well as in time, it was decided to perform simulations for Rayleigh numbers up to 10^{10} (2 orders of magnitude higher than the critical value) and to forget about details of transition to chaos. As usual, these simulations are started from a solution obtained at a lower Rayleigh number as the initial condition. It is thus necessary to integrate the unsteady Boussinesq equations long enough in time so that the transient effects have died out and the asymptotic state is reached. This requires an *a priori* knowledge of the time needed for the flow to reach its asymptotic state. It has been shown by Patterson & Imberger (1980), that for the laminar separated boundary layer regime, the approach to steady state is characterized by internal wave motion in the core and that the time needed to damp the waves which are generated in the transients is approximately $0.1 \times Ra^{0.5}$ in the time unit considered here, a very long time indeed. There is however no indication that this time scale is also the time needed to obtain the asymptotic motion in the fully chaotic regime and one should in fact anticipate a much smaller time scale for two reasons: first, large eddies of the chaotic motion enhance long-scale mixing by comparison with molecular viscous or thermal diffusion; second, and perhaps more importantly as will be shown below, internal wave motion becomes intrinsically part of the asymptotic motion in these fully chaotic regimes. Consequently, the time scale $0.1 \times Ra^{0.5}$, which is the time needed to damp these waves, becomes irrelevant for the flow regimes considered here. Our numerical experiments have indeed confirmed that this time scale is much smaller in the fully chaotic regime than for the steady laminar regime. When one feels confident that the asymptotic solution has been reached, one has furthermore to integrate long enough to obtain accurate time-averaged solutions and second-order statistics. Although it is not known for how long the unsteady Boussinesq equations have to be integrated in order that numerical results obtained be independent of time integration, it is clear that the higher the order of desired statistics the longer one has to integrate. Xin (1993) reported in detail the care taken in this respect and it was shown that at least the time-averaged fields we present below are time-integration independent. This required integrating the equations over a few hundreds of time

Ra	Spatial resolution	Time step	Total time
6.4×10^8	64×128	2.0×10^{-3}	400.0
2.0×10^9	64×256	1.5×10^{-3}	350.0
1.0×10^{10}	96×768	8.0×10^{-4}	250.0

TABLE 1. Calculation parameters

units which corresponds to several hundreds of thousands of time steps since the explicit treatment of the nonlinear convective terms results in a conditionally stable algorithm. For the largest value of the Rayleigh number that was investigated, the time step was 8×10^{-4}, and since the period of the basic travelling wave frequency in the boundary layers is approximately 0.4, this means that about 500 time steps are required for one travelling wave period. This ensures a very accurate time integration, which ensures a good accuracy of the low-order statistics (see Hussaini, Speziale & Zang 1989).

As far as spatial resolution is concerned, the number of Chebyshev polynomial has to be increased to resolve all the smallest scales of the flow, since otherwise the time integration becomes unconditionally unstable as is often the case with spectral methods. This results in a difficult situation, particularly and paradoxically enough in the vertical direction, since the transition point in the vertical boundary layers moves upstream with increasing Rayleigh number. Small structures are thus generated around the mid-cavity height, where the number of Chebyshev polynomials needed to resolve spatial scales of $O(\epsilon)$ varies like ϵ^{-1}. Small time steps and large spatial resolutions result in very expensive computations. To fix ideas, the integration at a Rayleigh number of 10^{10} has required more than 200 hours of CPU time on a VP200, which is a 500 MFlops class machine.

We list in table 1 spatial resolutions, time-step values and the total integration times used. For the largest Rayleigh number considered, we have used a 96×768 spatial resolution and integrated for a total time of 250 (in units of convective time). The time-averaged solutions and second-order statistics have been obtained over a time of 150, while Paolucci (1990) integrated from isothermal and quiescent conditions as initial condition for a total time of 100 and computed turbulent statistics over the final 30 time units in the square cavity at Ra of 10^{10}.

3.2. *Time-averaged flow structure*

Time-averaged fields are obviously important quantities for several reasons: they indicate the global structure of the flow and they are quantities which are computed in the conventional approaches to turbulence based on Reynolds averaging. In figure 1 we display the time-averaged solutions for values of Ra of 6.4×10^8, 2×10^9 and 10^{10}. These time-averaged fields were obtained by averaging over the total integration times indicated in figures 6, 7 and 8. Although the range of Rayleigh number investigated is relatively wide, it seems at first sight that these solutions differ very little. They share the usual flow features: thin vertical boundary layers, a stratified core region and recirculating structures near the downstream corners. A closer inspection reveals however that the solutions for the first two Rayleigh numbers still show basically the same flow structure as that found in the steady laminar regime, except perhaps the formation of a stronger recirculating flow region in the upper left corner of the cavity. On the other hand the flow structure for the highest Rayleigh number considered
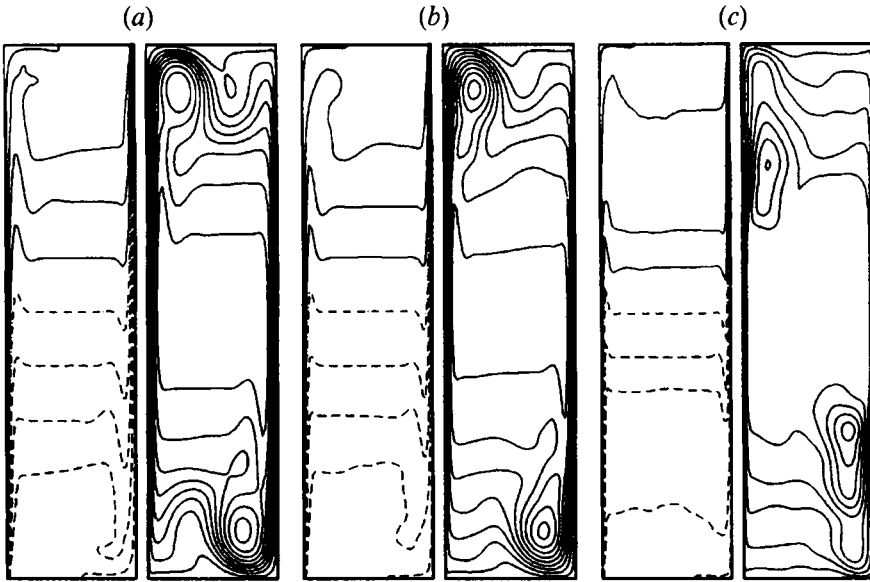
FIGURE 1. Time-averaged solutions: $Ra = 6.4 \times 10^8$ (*a*), 2×10^9 (*b*) and 10^{10} (*c*). For each solution the temperature is on the left and the streamlines are on the right. For temperature fields, the isovalues are ± 0.4, ± 0.3, ± 0.2, ± 0.1 and 0.0, while for the streamlines, the isovalues are respectively 0.0016, 0.0048, 0.008, 0.0112, 0.0144, 0.0176, 0.0208, 0.024 and 0.0272 for $Ra = 6.4 \times 10^8$, 0.0014, 0.0042, 0.007, 0.0098, 0.0126, 0.0154, 0.0182, 0.021 and 0.0238 for $Ra = 2. \times 10^9$, and 0.0012, 0.0037, 0.0062, 0.0087, 0.0112, 0.0137, 0.0162, 0.0187 and 0.0212 for $Ra = 10^{10}$.

is somewhat different from the other two. The recirculating structure has moved upstream and the boundary layer has also appreciably thickened in the downstream part. This sudden thickening corresponds to a strengthening of horizontal motion and a weakening of vertical motion – a sudden decrease of the wall shear stress (figure 2) in comparison with upstream flow. This happens at the location where the waves travelling downstream of the boundary layer have grown to a point where they totally disrupt these boundary layers and large eddies are ejected from the boundary layer. The location of this recirculating structure moves upstream with increasing Rayleigh number and for Ra of 10^{10} it is located in the mean around $z = 0.7$.

Likewise, examination of the temperature fields shows that the core region still displays a uniform stratification for the first two Rayleigh numbers. For the last one, the top and bottom parts of the core region become much more isothermal and the vertical temperature profile at mid-width (figure 3) shows that the vertical temperature gradient at mid-height is now larger than 1 (the average stratification is 1.2 in units of $\Delta T/H$ for $0.4 \leqslant z \leqslant 0.6$). This change in the structure of the temperature field is the result of the large unsteady eddies which are located in the mean around $z \approx 0.7$. These large eddies throw hot fluid into the upper parts of the core whereas hot fluid was thrown along the ceiling at a lower Ra value. The efficient mixing due to the large unsteady eddies results in almost isothermal hot upper and cold lower regions of the core respectively. Consequently most of the vertical temperature drop in the core occurs in a region around mid-height which shrinks as the Rayleigh number increases. An overall conclusion is that, over the range of Ra values investigated, the dimensionless stratification at mid-cavity height remains larger than 1 at Ra of 10^{10} which disagrees with what was observed by Paolucci (1990). Let us mention that this
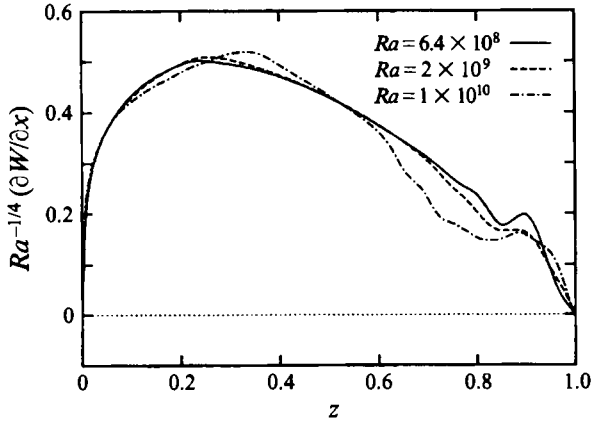
FIGURE 2. Dimensionless time-averaged wall shear stress $(\partial W/\partial x)$ scaled by $Ra^{1/4}$,
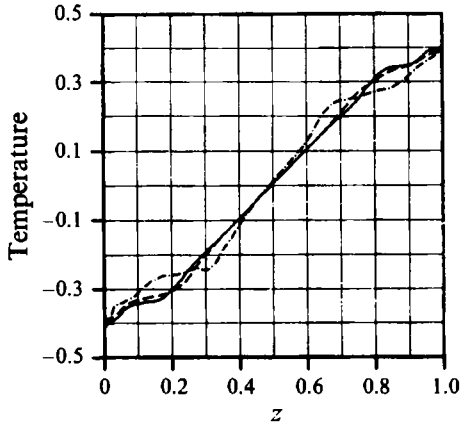i.e. $Ra^{-1/4} \times (\partial W/\partial x)$.

FIGURE 3. Vertical temperature profile at mid-width. Ra-values as figure 2.

discrepancy cannot be attributed to an aspect ratio effect, since the same result was later obtained in a square cavity (Le Quéré 1994a,b; Xin & Le Quéré 1994). The increased stratification observed for the largest Ra is however in good agreement with the fact that some solutions obtained with k-ϵ models also show such an increase of the stratification for Ra values in the range 10^9–10^{10} (Henkes 1990; Nobile *et al.* 1990; Le Breton 1991) before it eventually decreases to much smaller values (Henkes 1990). Let us also point out that the increase of stratification has never been observed in real experiments and is therefore probably strongly linked to the assumption of adiabatic top and bottom walls, which are academic boundary conditions that are never met in practice. In experimental set-ups, the actual boundary conditions which have been measured show that the temperature distribution corresponds to boundary conditions between adiabatic walls and perfectly conducting walls (Mergui *et al.* 1992). Another possible source of discrepancy is obviously three-dimensional effects.

Profiles of the time-averaged vertical velocity component at several vertical positions are displayed in figure 4. They show that the velocity maxima remain constant and that the boundary layers get thinner as Ra increases. The right-hand sides of the figure also show that, when scaled with $Ra^{1/4}$, all profiles over the first 60% of the
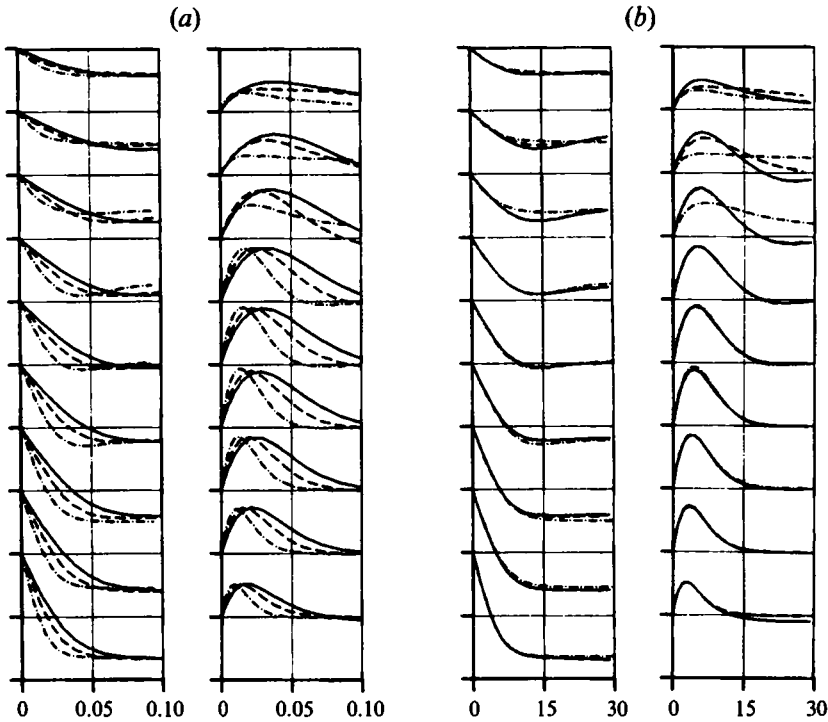
FIGURE 4. Temperature (*a*) and vertical velocity (*b*) profiles at $z = 0.1, 0.2, 0.3, 0.4, 0.5, 0.6, 0.7, 0.8$ and 0.9 (from bottom to top) for $Ra = 6.4 \times 10^8$ (———), 2×10^9 (——) and 10^{10} (— · —). For the plots on the left, the abscissa is $4x$ (i.e. the dimensionless width is 1) whereas for the plots on the right, the abscissa is $4xRa^{1/4}$.

boundary layer collapse on the same profile. This confirms that even for the highest Ra investigated more than half of the vertical boundary layer is still laminar or quasi-laminar.

It would obviously be of utmost interest to check the validity of the scaling laws proposed by George & Capp (1979), who derived $-\frac{1}{3}$ and $\frac{1}{3}$ power laws respectively for temperature and vertical velocity in the buoyant sublayer. These laws were established under the assumption of fully developed turbulent boundary layers and it is clear that, even for the largest Ra value of 10^{10}, the flow regime has not yet reached such a state of developed turbulence. We therefore believe that such a comparison is not very meaningful for the present results.

3.3. *Flow dynamics*

3.3.1. *Instantaneous flows*

We have discussed so far the global characteristics of the flow structure given by the time-averaged fields, which increasingly depart from the corresponding structure for the laminar regime. In addition the direct simulations give access to the instantaneous features of the flow and temperature fields and give some insight into the dynamics of chaotic natural convection and the physical mechanisms involved.

Time sequences of instantaneous temperature fields visualized in interferogram form are displayed in figure 5. At $Ra = 6.4 \times 10^8$, which is 6 times above the critical value, one notes periodic oscillations of the isotherms in the downstream parts of the boundary layers, which corresponds to the primary instability mechanism, in the
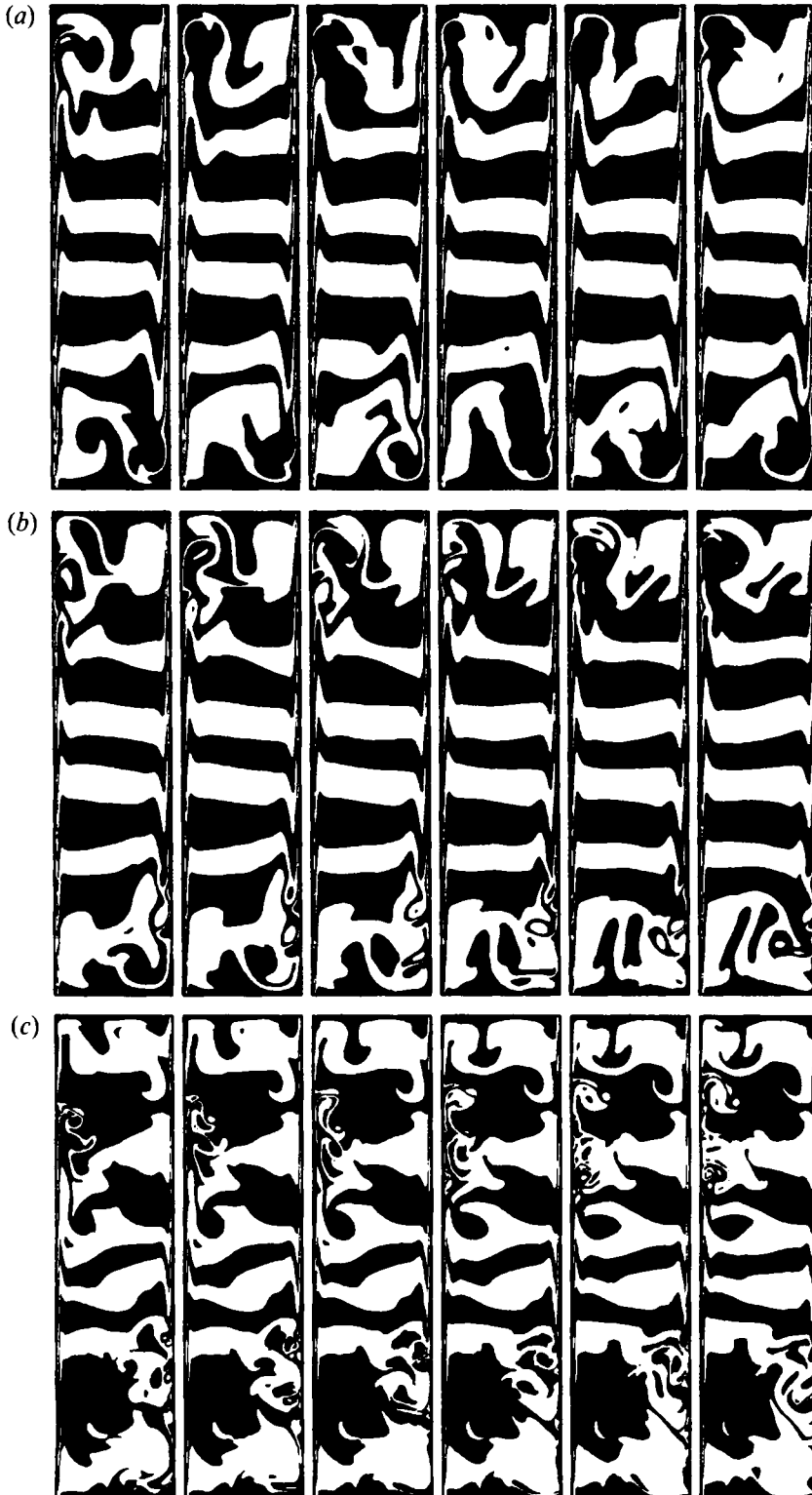
(a)

(b)

(c)

FIGURE 5. Time sequence of instantaneous temperature fields at (a) $Ra = 6.4 \times 10^8$, (b) $Ra = 2 \times 10^9$, (c) $Ra = 10^{10}$.

form of Tollmien–Schlichting waves. One also notes that rather large fluctuations are observed in the two downstream corners of the cavity, but the cavity core is still motionless and well stratified. Despite the large fluctuations which invade the top and bottom parts of the cavity core and which correspond to time signals which are very chaotic, the flow is far from what can be called turbulent. At $Ra = 2 \times 10^9$, the oscillations of isotherms in the downstream part of the boundary layer become more irregular and large eddies are formed there and ejected into the cavity core. The stratified cavity core is no longer motionless and the isotherms oscillate periodically around their mean horizontal position. At $Ra = 10^{10}$ both phenomena become more marked: large eddies appear around $z = 0.6$ near the hot vertical wall and most of the cavity core is in motion. With increasing Ra the cavity core thus appears increasingly disorganized and the region of uniform stratification shrinks accordingly. This seems to contradict Paolucci's finding of a relatively quiescent and weakly stratified core region in the square cavity. As can be seen, large chaotic eddies invade the core region at the highest Rayleigh number, but the boundary layers remain almost laminar in their upstream part which agrees very well with the experimental results of Giel & Schmidt (1990) in a cavity of aspect ratio 10 filled with water. The large eddies which are ejected from the boundary layers result in the formation of hook-like patterns of the temperature field which have also been found experimentally and numerically (Steinberner & Reineke 1978; Paolucci 1990).

3.3.2. *Time traces, power spectra and probability density distributions*

Typical time traces of temperature and velocity that will be presented in the following correspond to points labelled A ($A \times x = 0.147, z = 0.85$), B ($A \times x = 0.038, z = 0.85$) and D ($A \times x = 0.038, z = 0.778$) for the two extreme Rayleigh values of 6.4×10^8 and 10^{10} and A, B and C ($A \times x = 0.038, z = 0.725$) for the intermediate value of 2×10^9. These points are located in the downstream part of the hot boundary layer and it can be seen from figure 4 that B, C, D are located around the location of the velocity maximum while A, which is at the same elevation than B, is located at the outer edge of the boundary layer. At a Rayleigh number of 6.4×10^8, the high frequency of the sidewall boundary-layer instability still clearly shows up in the time signals (figure 6) despite the chaotic behaviour. One however notices that the time traces at point A clearly exhibit an intermittent character: the high-frequency travelling wave boundary layer instability is modulated by a very low frequency. As low-frequency phenomena correspond to large structures, the very low frequency is possibly due to the weak motion which takes place in the top part of cavity core. Time signals obtained at A, B and C for a Rayleigh number of 2×10^9 are displayed in figure 7. At point C, which is located most upstream, despite the presence of very large fluctuations, the signals display the high-frequency oscillations characteristic of the travelling wave instability. These high-frequency oscillations are still visible intermittently at point B further dowstream, but it is clear that the signals are now characterized by fluctuations of much smaller frequency. At point A, which is almost in the core, the high-frequency oscillations are almost never seen and the signals are dominated by very low-frequency intermittent oscillations. The origin of these very low-frequency oscillations at points B and A is linked to the formation of the large eddies which are ejected from the boundary layer into the core, and this Rayleigh value really corresponds to the onset of the fully chaotic regime. For the highest Rayleigh number considered, the high frequency of sidewall instability has almost completely disappeared from the temperature and velocity traces (figure 8) at
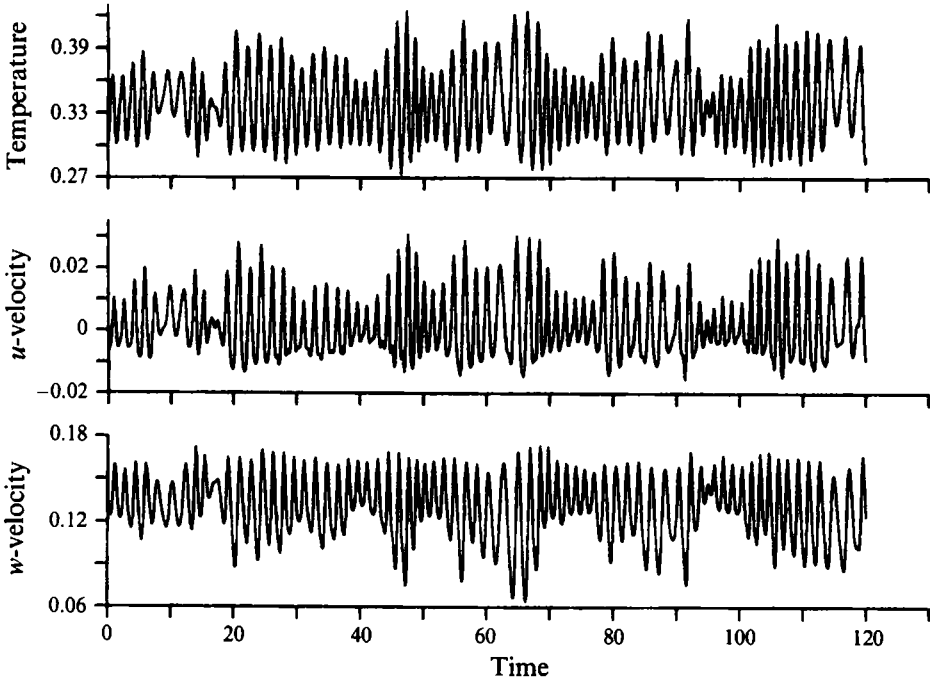
S. Xin and P. Le Quéré

(a)
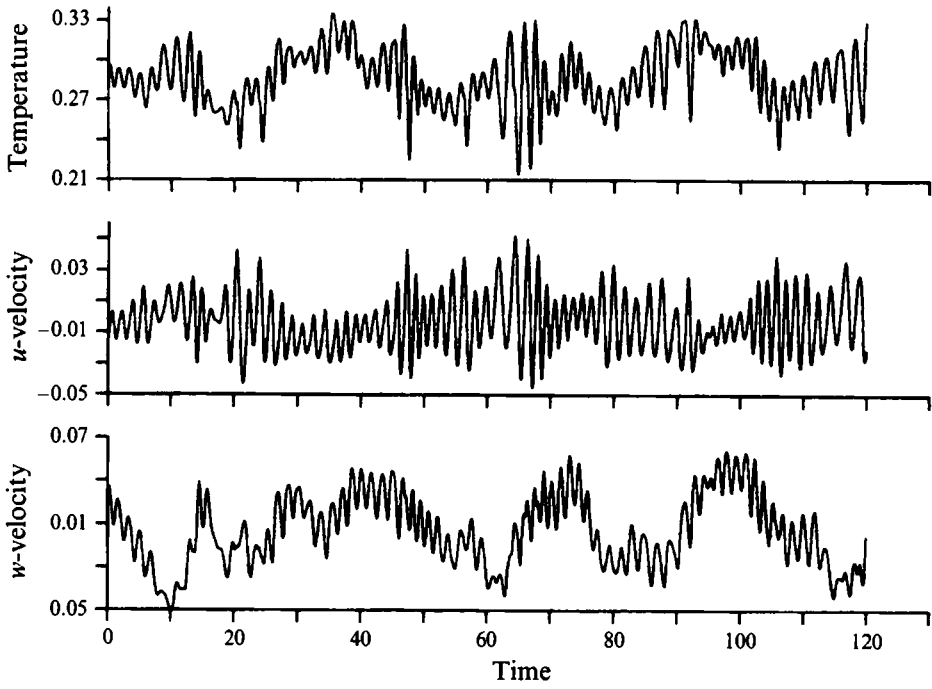
(b)

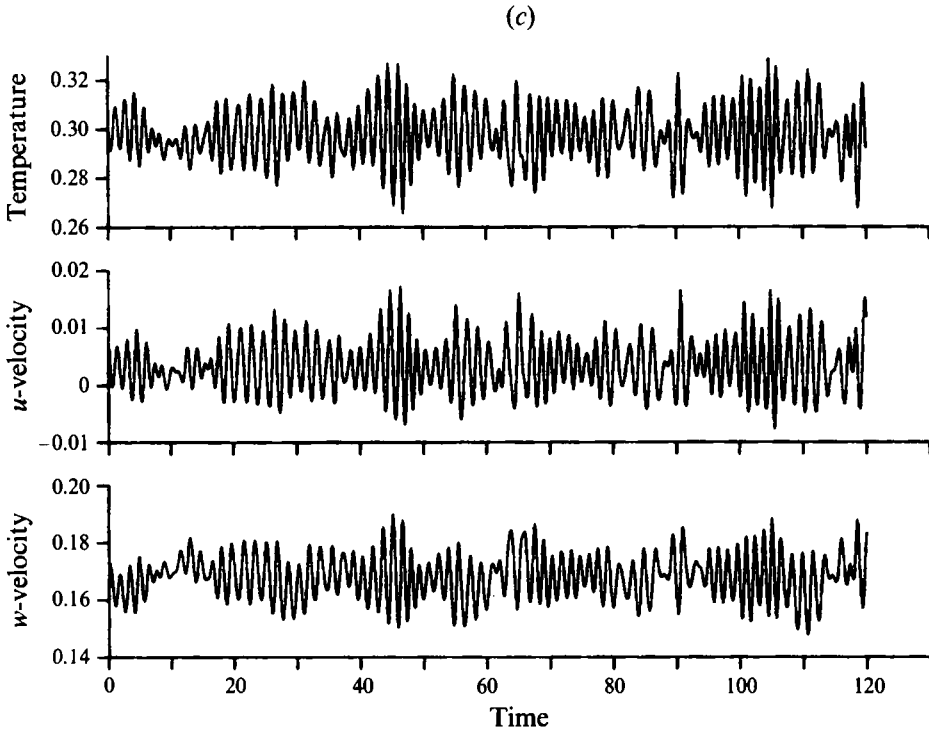FIGURE 6 (a,b). For caption see facing page.

(c)

FIGURE 6. Time traces of temperature and velocity at (a) A ($4x = 0.147$, $z = 0.8535$), (b) B ($4x = 0.038$, $z = 0.8535$), (c) D ($4x = 0.038$, $z = 0.778$): $Ra = 6.4 \times 10^8$.

the given monitoring locations because these points are located downstream of the location where large eddies have been generated and expelled into the core.

To summarize, with increasing Rayleigh number, time traces of temperature and velocity become increasingly chaotic. The increased irregularity in the signals is due to the fact that the same dimensionless position in the cavity corresponds to physical locations of increasing local Rayleigh number at which instabilities have reached different stages in their development and the high frequency of sidewall instability disappears in the downstream part of the boundary layer because of the large eddies which completely tear up the boundary layer and the travelling waves.

Density power spectra of the temperature traces are displayed in figures 9 and 10 for Rayleigh numbers of 2×10^9 and 10^{10}. These power spectra show broadband components with no really predominant frequency and a large part of the energy is contained in low-frequency modes. For $Ra = 2 \times 10^9$, at A and B the high-frequency sidewall instability does not show up in the spectrum although it can be seen in the corresponding time traces. This frequency however shows up at the lowest location C but we also note the importance of some low frequencies corresponding to the very large but rare fluctuations. As indicated by the time traces, at Ra of 10^{10} the high frequency is not observed at A, B and D. Low frequencies contain the major part of the energy of the signals. The power spectra of the velocity signals yield the same conclusions.

In figures 11 and 12 are displayed the probability density distributions of temperature and velocity obtained for the two highest Rayleigh numbers investigated at the selected locations: A, B, C and D. The probability density distribution, $P(f_0)$, of a
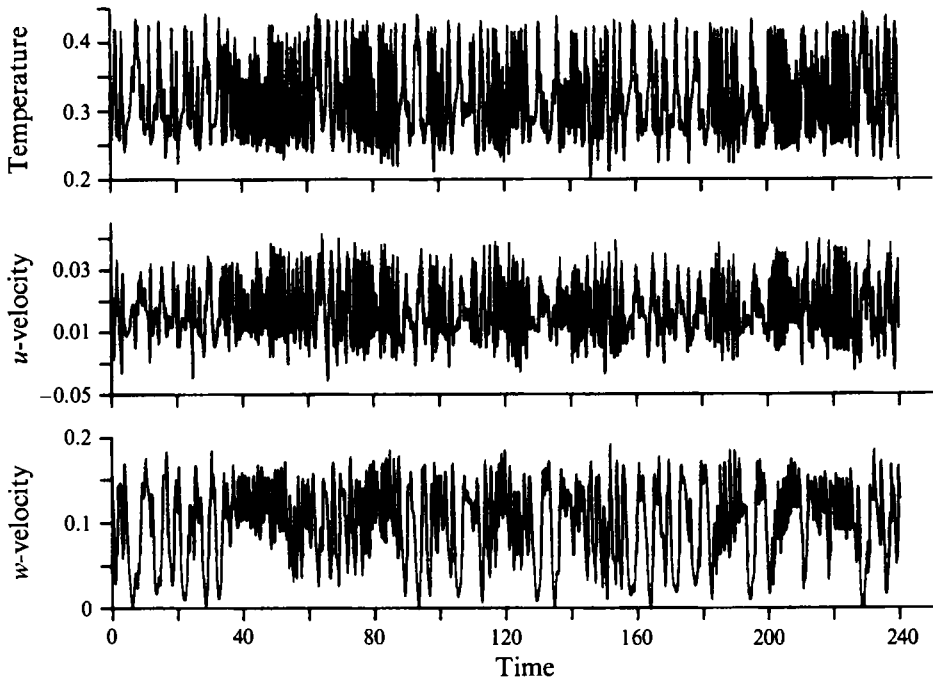
(a)
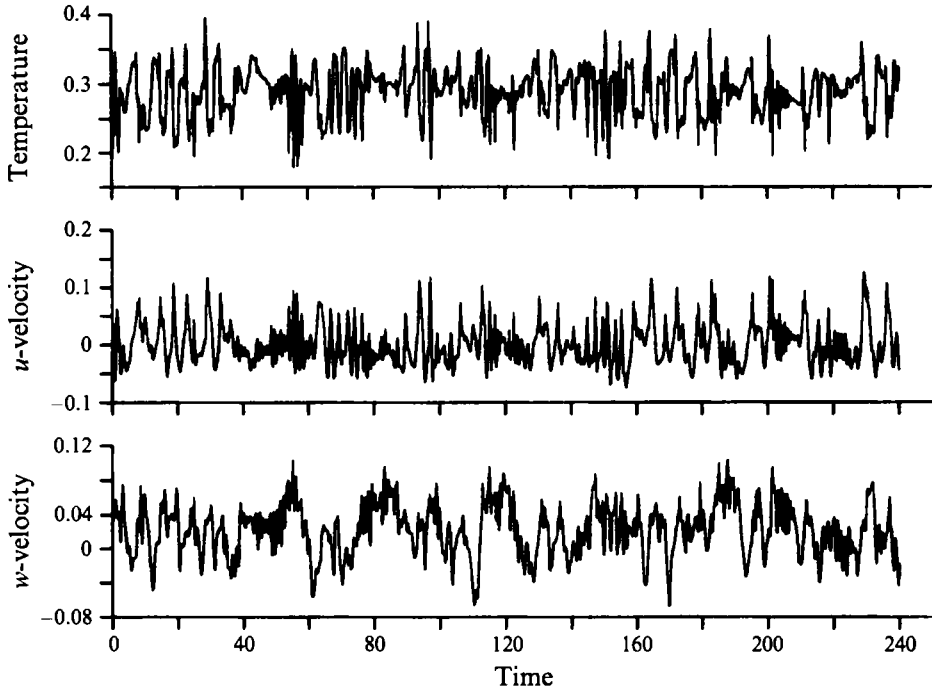
(b)

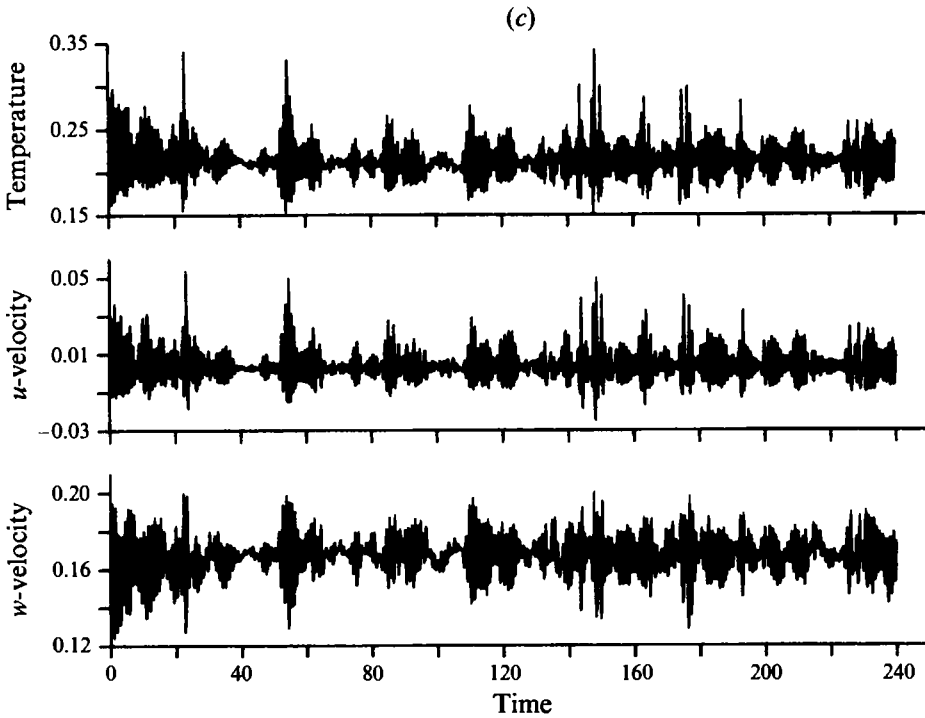

FIGURE 7 (a,b). For caption see facing page.

(c)

FIGURE 7. Time traces of temperature and velocity at (a) A ($4x = 0.147$, $z = 0.8535$), (b) B ($4x = 0.038$, $z = 0.8535$), (c) C ($4x = 0.038$, $z = 0.725$): $Ra = 2. \times 10^9$.

time trace $f(t)$, is defined as the fraction of the time where $f_0 \leqslant f \leqslant f_0 + \mathrm{d}f$ and one has $\int_{-\infty}^{\infty} P(f)\,\mathrm{d}f = 1$. It is clear from figures 11 and 12, in which the vertical lines indicate the time-averaged values, that the probability density distributions are not symmetrical with respect to the time-averaged values because the cavity walls and the stratification in the cavity core region are important sources of flow anisotropy. In particular wall effects are clearly seen in the p.d.f. of u, the horizontal component of velocity. We first note that the value of u corresponding to the maximum probability density is smaller than the time-averaged value and that the largest negative fluctuations are smaller than the positive ones. It is also noted that the time-averaged values are very close to zero since close to the wall the fluid flows vertically and negative fluctuations thus correspond approximately to the negative u values. It is thus clear that the presence of the wall prevents the occurrence of large negative fluctuations of u whereas there is no such constraint on the positive ones. This explains why u spends most time at a level lower than the time-averaged value so as to balance the largest positive fluctuations.

3.3.3. *Internal waves*

Figure 5 shows that for the highest two Rayleigh numbers considered most of the cavity core is in motion and the isotherms in the core oscillate around their mean horizontal position. Since the cavity core is well stratified this phenomenon can tentatively be ascribed to internal waves and it is therefore suggested that the large-amplitude fluctuations due to the sidewall boundary layer instability are capable of permanently exciting the internal waves which oscillate at their characteristic
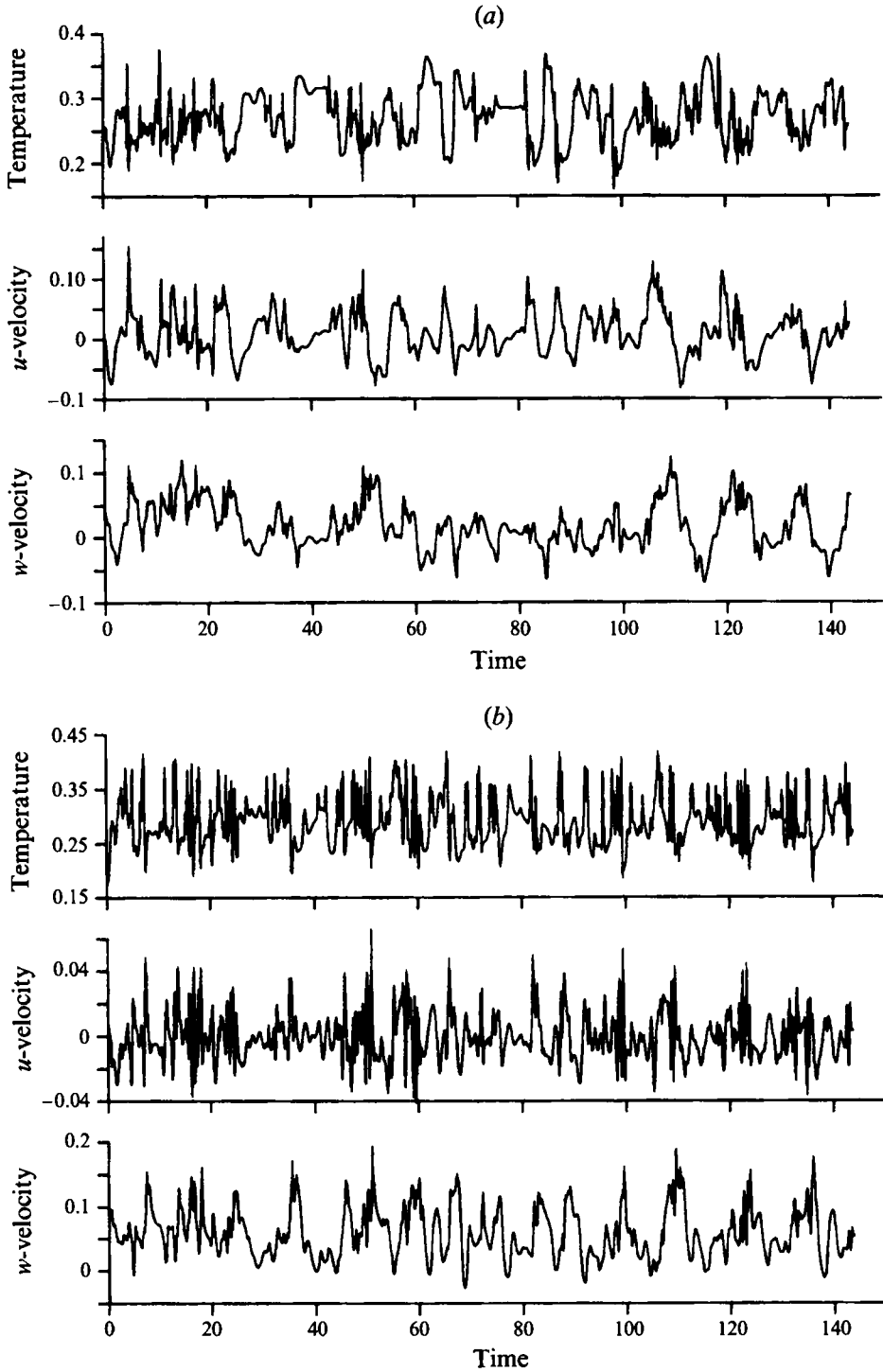
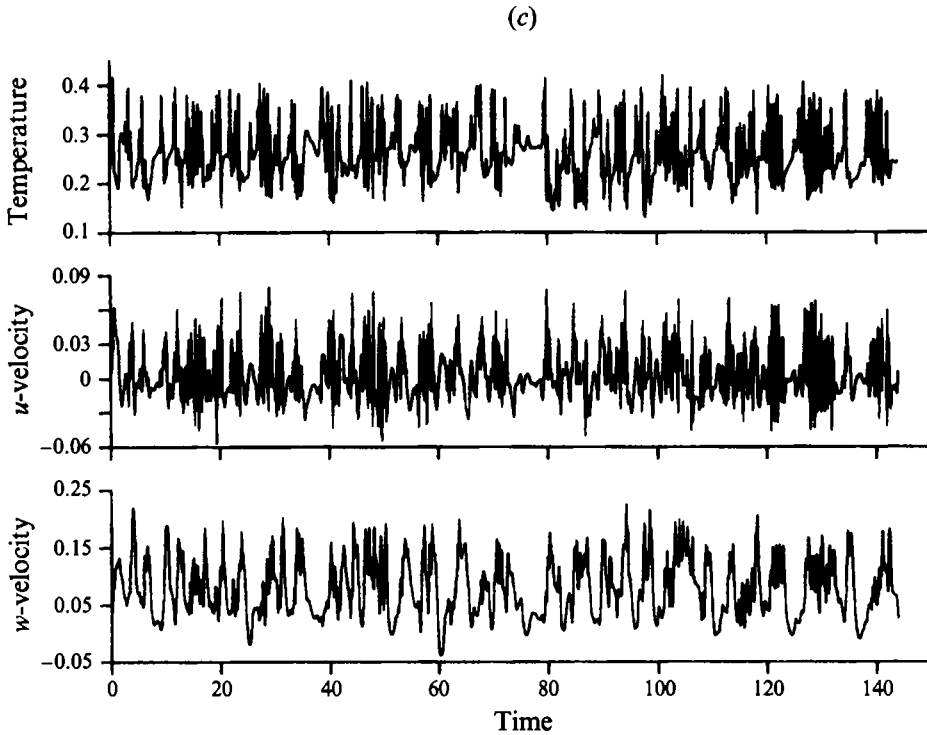FIGURE 8 (*a,b*). For caption see facing page.

(*c*)

FIGURE 8. Time traces of temperature and velocity at (*a*) A ($4x = 0.147$, $z = 0.8535$),
(*b*) B ($4x = 0.038$, $z = 0.8535$), (*c*) D ($4x = 0.038$, $z = 0.775$): $Ra = 10^{10}$.

frequency. Patterson & Imberger (1980) indeed showed that the stratified core region of the cavity is capable of sustaining internal wave oscillations, which, if not permanently forced, are damped through viscous effects. This assumption can be checked by looking at the mean Nusselt number Nu_c through the vertical mid-plane, which is known to well characterize the wave motion in the core. Time traces of Nu_c, displayed in figure 13, indeed exhibit almost periodic oscillations and the fundamental frequencies obtained from their power spectra are 0.130 for $Ra = 2 \times 10^9$ and 0.137 for $Ra = 10^{10}$. These oscillation frequencies should be compared with the characteristic dimensional Brunt–Väisälä frequency: $f_{BV} = (g\beta C\Delta T/H)^{0.5}/(2\pi)$ where C is the dimensionless stratification of the time-averaged temperature fields in the core region (measured in units of $\Delta T/H$). In the present time unit, the dimensionless Brunt–Väisälä frequency reads: $N = (CPr)^{0.5}/(2\pi)$. Taking into account the actual stratification in the core, the dimensionless Brunt–Väisälä frequency is 0.134 for $Ra = 2 \times 10^9$ and 0.147 for $Ra = 10^{10}$. The agreement between both sets of values is good and supports the assertion that internal waves do get permanently excited by the waves propagating in the sidewall boundary layers, or perhaps more accurately, by the large structures which are ejected from the boundary layers.

This is to our knowledge the first clear evidence that the excited internal wave motion is intrinsically part of the asymptotic flow regime. It means that the excitation of the internal waves is certainly one of the characteristic features of fully chaotic natural convection in differentially heated cavities. Although the role played by internal waves in these flows is still not clear, it is certainly very important. As pointed out by Stuhmiller (1979), turbulent buoyant flows in a gravitational field
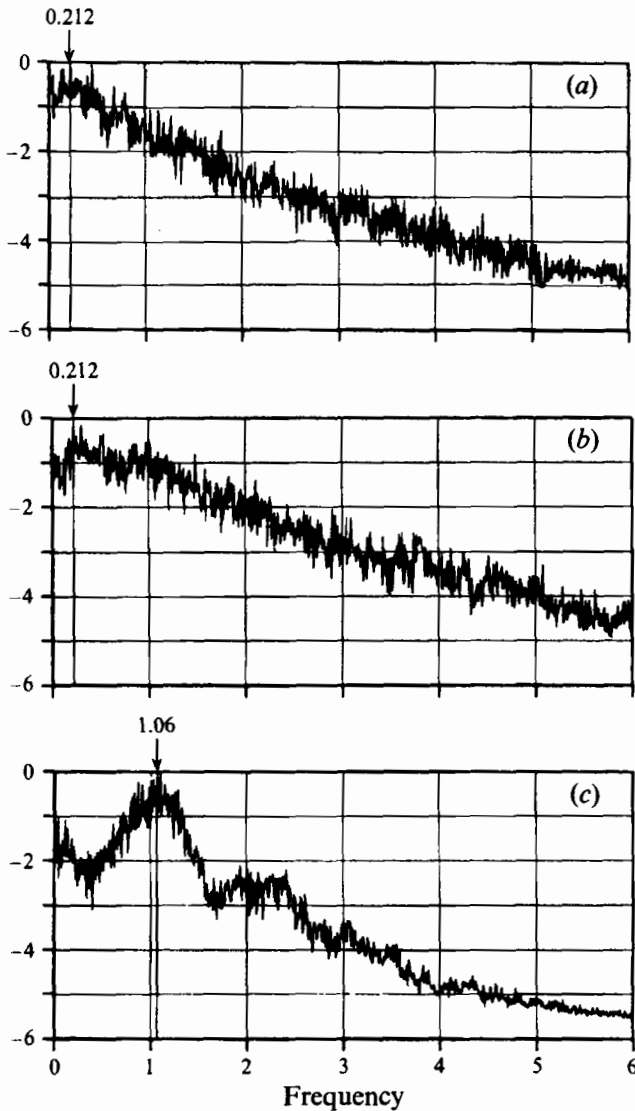
FIGURE 9. Density power spectra of temperature at (a) A, (b) B and (c) C for $Ra = 2 \times 10^9$.

possess the following unique characteristics: the presence of internal waves; flow anisotropy created by stratification, resulting in a preferred direction of fluid motion; and a tendency to a two-dimensional structure. Since it is well known that internal wave motions are dispersive but only weakly dissipative, the passage of an internal wave through a stably stratified region has no effect on the density profile but internal waves do interact with non-wave flows and cause a momentum exchange and therefore an energy exchange. It would thus be of interest to determine how much energy is carried by the internal waves in comparison with the energy that cascades to the small scales. The answer to this question will tell us whether this feature needs to be taken into account in the turbulence models developed for differentially heated cavities, as has been done for other configurations (Uitenborgaard & Baron 1989).

It is still not clear at which Rayleigh value these internal waves get excited for the first time. It is well known that if one excites a linearly stratified fluid at rest with a
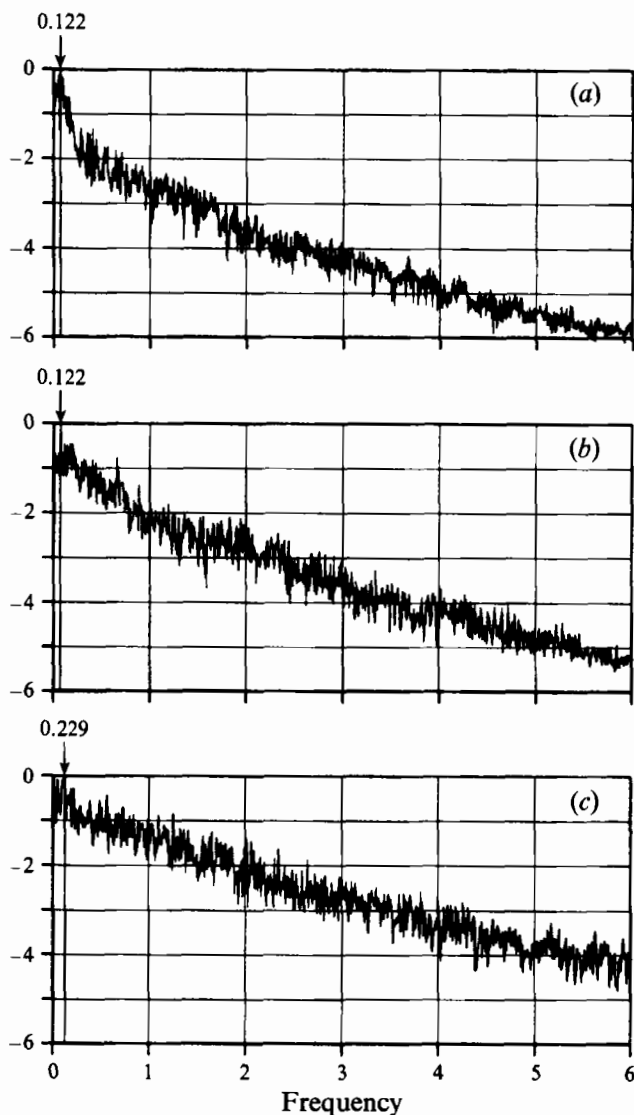
FIGURE 10. Density power spectra of temperature at (*a*) A, (*b*) B and (*c*) D for $Ra = 10^{10}$.

frequency ω, internal waves are generated only if $\omega \leqslant N$ and the dispersion relation reads $\omega^2 = N^2(1 - k_z^2/k^2)$, where k_z is the vertical component of the wave vector k. These waves then propagate at an angle θ such that $\theta = \arccos(\omega/N)$ (see e.g. Lighthill 1978 or Craik 1985). The Brunt–Väisälä frequency is thus the maximum frequency of the internal waves that can be observed. In our case the forcing mechanism is due to the travelling wave instability of the vertical boundary layers, which are characterized, when they first appear, by a dimensionless frequency larger than the Brunt–Väisälä frequency, and cannot therefore excite the internal waves. This is to be contrasted with what happens in a square cavity in which the first instability is characterized by a dimensionless frequency smaller than the Brunt–Väisälä frequency and in which internal waves can be observed in the core region right at the onset of unsteadiness (see Le Quéré & Behnia 1994). In the present configuration, one has therefore to increase the Rayleigh number up to a point when successive bifurcations

(a)

(b)

(c)

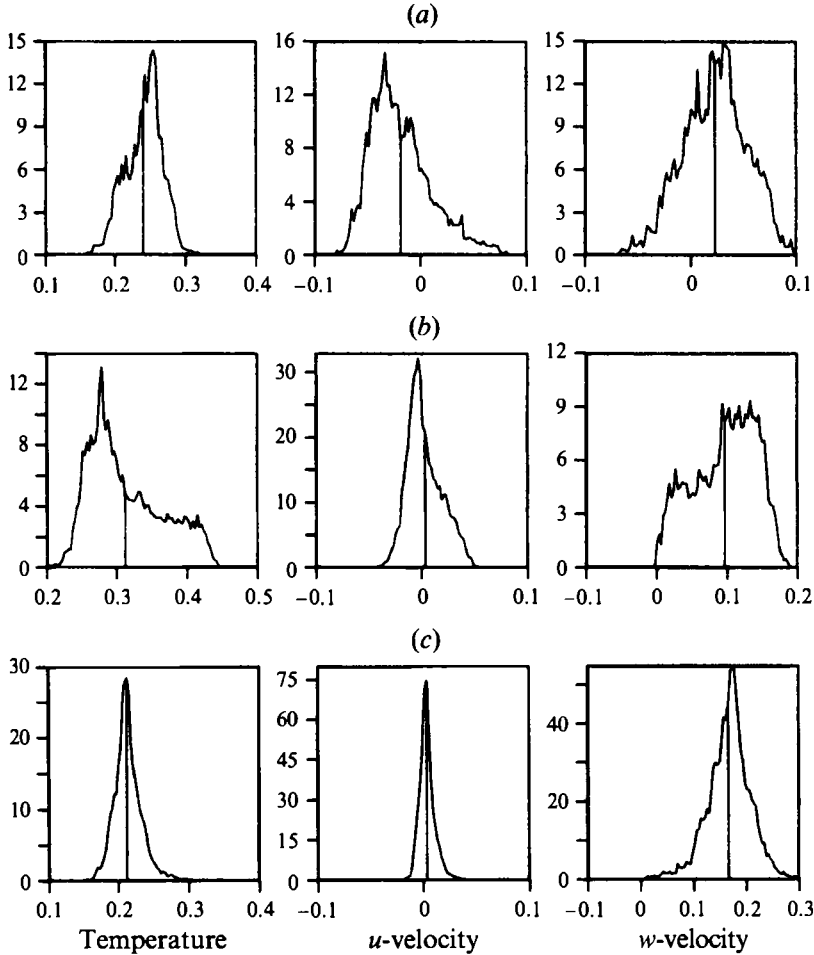Temperature   *u*-velocity   *w*-velocity

FIGURE 11. Probability density distribution at (a) A, (b) B and (c) C for $Ra = 2 \times 10^9$.

and nonlinear interactions have produced frequencies in the time spectra smaller than the Brunt–Väisälä frequency. In other words this corresponds to the appearance of eddies of sufficiently large scale so as to be characterized by frequencies smaller than the Brunt–Väisälä frequency. It is thus clear that the permanent excitation of the internal waves is due to the large eddies which are the result of the non linear interactions of the travelling waves in the boundary layers. This drain of energy from the eddies to the internal waves probably has important consequences for the dynamics of the solution and its turbulent characteristics.

3.4. 'Turbulent' statistics

Second-order statistics have been computed for the two simulations at the highest Rayleigh numbers over integration periods corresponding to the time evolutions shown in figures 7 and 8. Because these simulations are only two-dimensional and it is quite clear that the flow is not yet in a state which is fully turbulent, the results presented in this section should be taken qualitatively and as an assessment of the methodology. They nevertheless can give some indications of the magnitude of the fluctuating components and of some spatial correlations.

Figures 14 and 15 present respectively for $Ra = 2 \times 10^9$ and $Ra = 10^{10}$ the
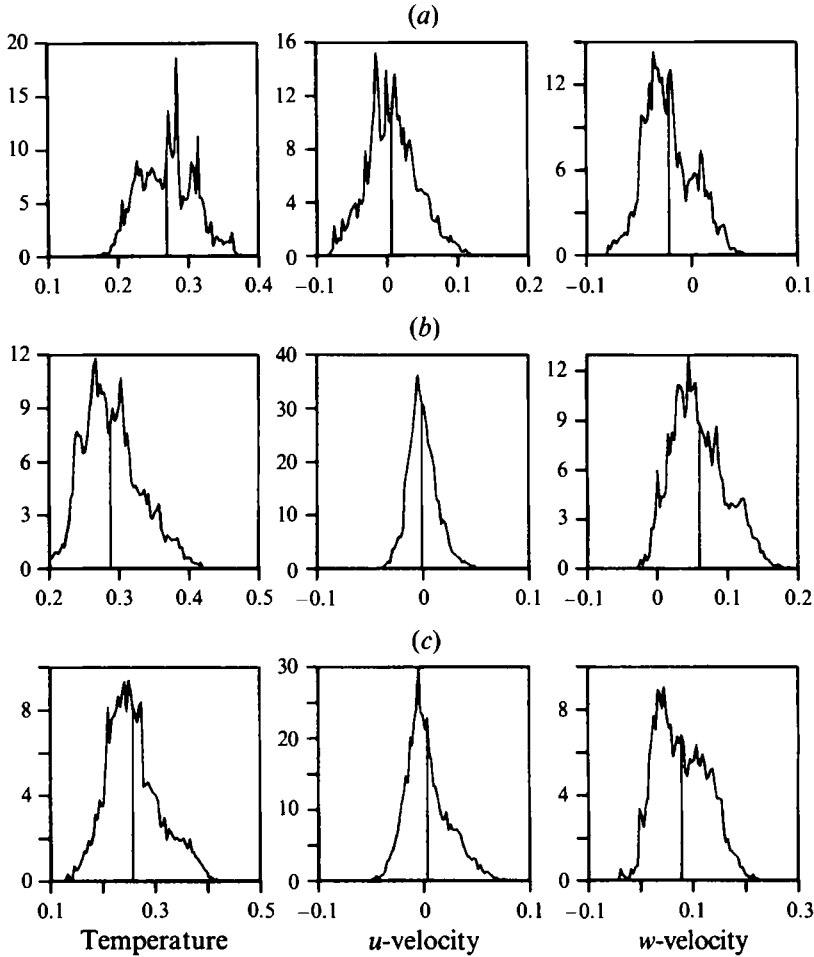
FIGURE 12. Probability density distribution at (*a*) A, (*b*) B and (*c*) D for $Ra = 10^{10}$.

Reynolds stresses, the temperature variance $\overline{\Theta'^2}$, the turbulent kinetic energy $k = \frac{1}{2}\overline{u_i'u_i'}$, its viscous dissipation rate $\epsilon_v = \overline{(\partial u_i'/\partial x_j)^2}$, the turbulent thermal dissipation $\epsilon_\Theta = \overline{(\partial \Theta'/\partial x_j)^2}$ and the turbulent heat fluxes $\overline{u_i'\Theta'}$. These plots confirm, as expected, that these characteristic quantities of 'turbulent' fluctuations are only significant in the downstream part of vertical boundary layers. They also make clear that, even for what can be considered as a large Ra value, an important part of the flow – the upstream part of the boundary layer and a large part of the core – remains laminar. This seems typical of this type of configuration for a large range of practical applications and refined turbulence models should be able to predict this feature without too much *a priori* knowledge on the location of the transition point. They show that the turbulence intensity increases with Ra and so does the region of 'turbulent' fluctuations larger than a given threshold. They also show that, as Ra increases, because the transition point of boundary layers moves upstream the location of maxima of $\overline{u'^2}$, $\overline{w'^2}$, turbulent kinetic energy, $\overline{\Theta'^2}$, ϵ_v and ϵ_Θ moves upstream, but the maxima of viscous turbulent dissipation and thermal dissipation always remain at the vertical walls.

It is clear from the plots that the pairs $(\overline{w'^2}, \overline{\Theta'^2})$, $(\overline{w'^2}, \epsilon_v)$, $(\overline{\Theta'^2}, \epsilon_\Theta)$ and $(\epsilon_v, \epsilon_\Theta)$ are well correlated in space whereas the pairs $(\overline{u'^2}, \overline{w'^2})$ and (k, ϵ_v) are not. $\overline{w'^2}$ and

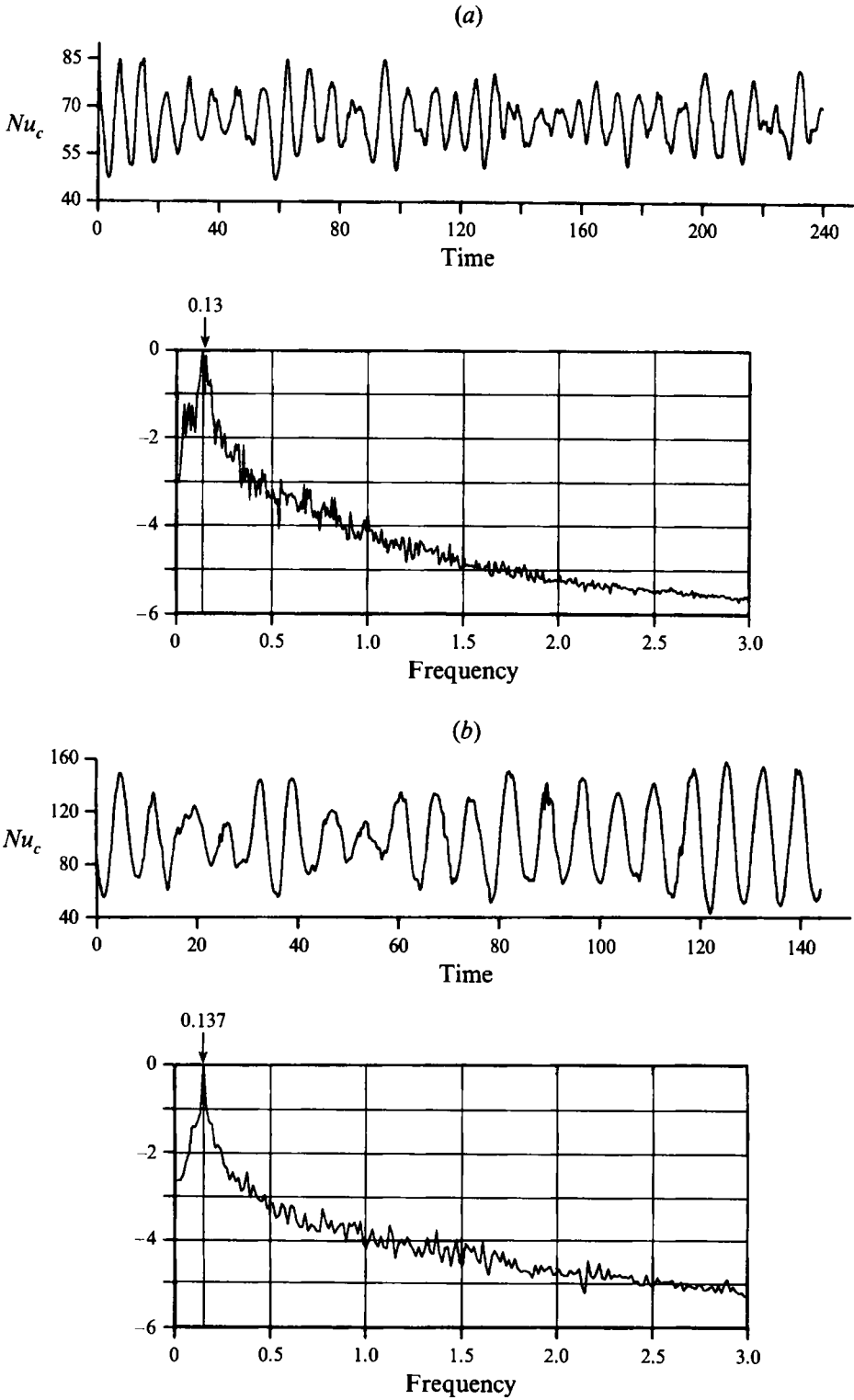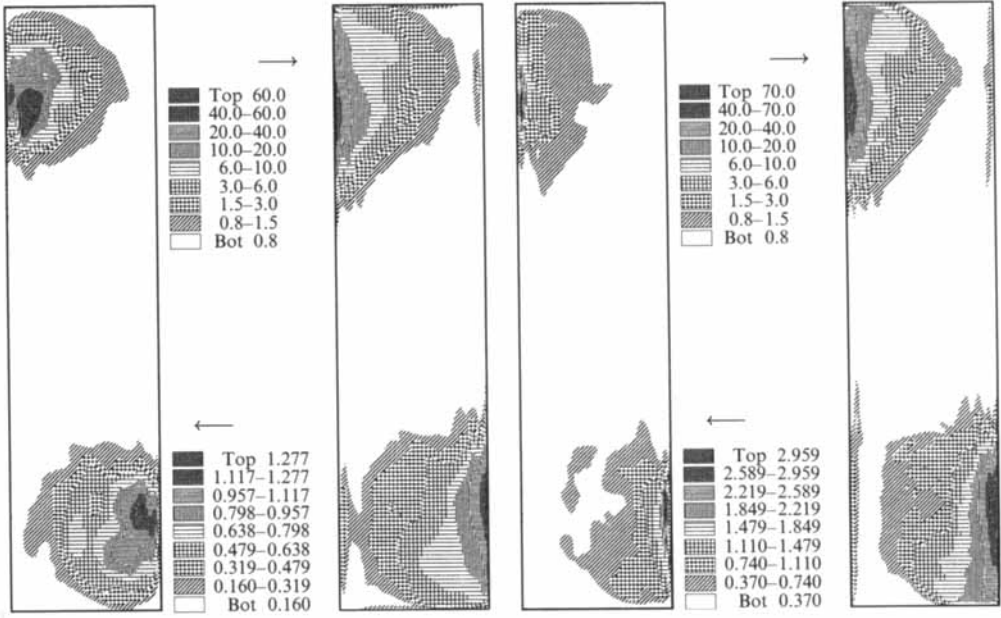S. Xin and P. Le Quéré

(a)

(b)

FIGURE 13. Time traces of Nusselt number at the vertical mid-plane ($Ra = 2 \times 10^9$ (a) and $Ra = 10^{10}$ (b)) and the corresponding power spectra.

(a)

Top 60.0
40.0–60.0
20.0–40.0
10.0–20.0
6.0–10.0
3.0–6.0
1.5–3.0
0.8–1.5
Bot 0.8

Top 70.0
40.0–70.0
20.0–40.0
10.0–20.0
6.0–10.0
3.0–6.0
1.5–3.0
0.8–1.5
Bot 0.8

Top 1.277
1.117–1.277
0.957–1.117
0.798–0.957
0.638–0.798
0.479–0.638
0.319–0.479
0.160–0.319
Bot 0.160

Top 2.959
2.589–2.959
2.219–2.589
1.849–2.219
1.479–1.849
1.110–1.479
0.740–1.110
0.370–0.740
Bot 0.370

(b)

Top 1.934
1.693–1.934
1.451–1.693
1.209–1.451
0.967–1.209
0.725–0.967
0.484–0.725
0.242–0.484
Bot 0.242

Top 1.498
1.311–1.498
1.123–1.311
0.936–1.123
0.749–0.936
0.562–0.749
0.374–0.562
0.187–0.374
Bot 0.187

Top 0.300
0.200–0.300
0.150–0.200
0.100–0.150
−0.100–0.100
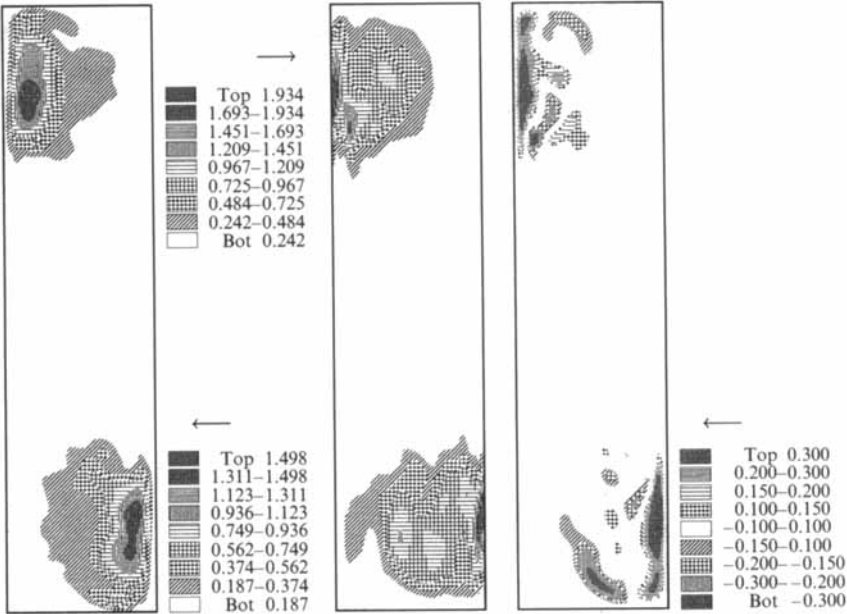−0.150–0.100
−0.200–−0.150
−0.300–−0.200
Bot −0.300

FIGURE 14 (*a,b*). For caption see next page

$\overline{\Theta'^2}$ possess their maxima near the vertical walls, while the location of maximum amplitude of $\overline{u'^2}$ is well outside the boundary layer. This shows that the anisotropy of the velocity fluctuations (very close to the walls u' behaves as x^2 but w' as x where x is the distance to the wall) extends well outside the viscous sub-layer. Sufficiently close to the wall, due to the anisotropy behaviour and the Dirichlet boundary conditions of
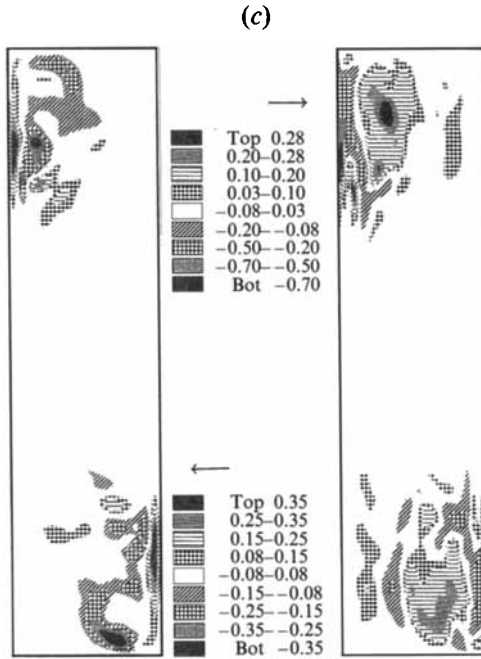
(c)

FIGURE 14. (a) Turbulent statistics at $Ra = 2 \times 10^9$; from left to right: k, ϵ_v, $\overline{\Theta'^2}$ and ϵ_Θ. k and $\overline{\Theta'^2}$ should be multiplied by 10^{-3}. The maximum values for ϵ_v and ϵ_Θ are 430 and 130. (b) Turbulent statistics at $Ra = 10^{10}$: $\overline{u'^2}$, $\overline{w'^2}$ and $\overline{u'w'}$ (from left to right). The scale of the Reynolds stresses should be multiplied by 10^{-3}. (c) Turbulent statistics at $Ra = 10^{10}$: $\overline{u'\Theta'}$ and $\overline{w'\Theta'}$ (from left to right). The scale of the turbulent heat fluxes should be multiplied by 10^{-3}.

velocity components, the viscous dissipation rate ϵ_v is mainly contributed by $\partial w'/\partial x$. Since at the vertical walls Θ' is zero, the same is also true for the thermal dissipation rate, because close to the isothermal vertical walls, the leading term of the thermal dissipation is given by $\overline{(\partial \Theta'/\partial x)^2}$. As k is contributed to by u' and w', its maximum follows approximately that of $\overline{u'^2}$ and since ϵ_v is essentially contributed to by $\partial w'/\partial x$, one easily understands the origin of the bad spatial correlation between k and ϵ_v.

The turbulent kinetic energy k and its viscous dissipation rate ϵ_v are generally two key quantities in turbulence modelling. In particular, for computations which extend throughout to the wall, the ϵ_v-equation requires boundary conditions. Jones & Launder (1972, 1973) have shown that these can be obtained from a kinematic relationship between k and ϵ, which in dimensionless form reads $\epsilon_w = 2(\partial k^{0.5}/\partial x)^2_w$. Our numerical results reproduce this analytical kinematic relationship with a relative error of less than 0.1% (Xin 1993). This agreement, which concerns derivatives of the primary variables, furthermore indicates that the second-order statistics which have been obtained seem reliable.

Figures 14 and 15 also show that $\overline{u'w'}$, $\overline{u'\Theta'}$ and $\overline{w'\Theta'}$ are relatively small since their maxima are two or three times smaller than those of $\overline{u'^2}$, $\overline{w'^2}$ and $\overline{\Theta'^2}$. Roughly speaking, $\overline{u'w'}$ and $\overline{u'\Theta'}$ are positive in the near-wall region and negative in the far region, while $\overline{w'\Theta'}$ is negative in the near-wall region and positive in the far region. k-ϵ type modelling generally makes use of a Boussinesq-type relationship: $\overline{u'w'} = -\nu_t(\partial \overline{u}/\partial z + \partial \overline{w}/\partial x)$, $\overline{u'\Theta'} = -(\nu_t/\sigma_t)\partial \overline{\Theta}/\partial x$ and $\overline{w'\Theta'} = -(\nu_t/\sigma_t)\partial \overline{\Theta}/\partial z$ where ν_t is the eddy viscosity, σ_t is the turbulent Prandtl number and the overbarred quantities are
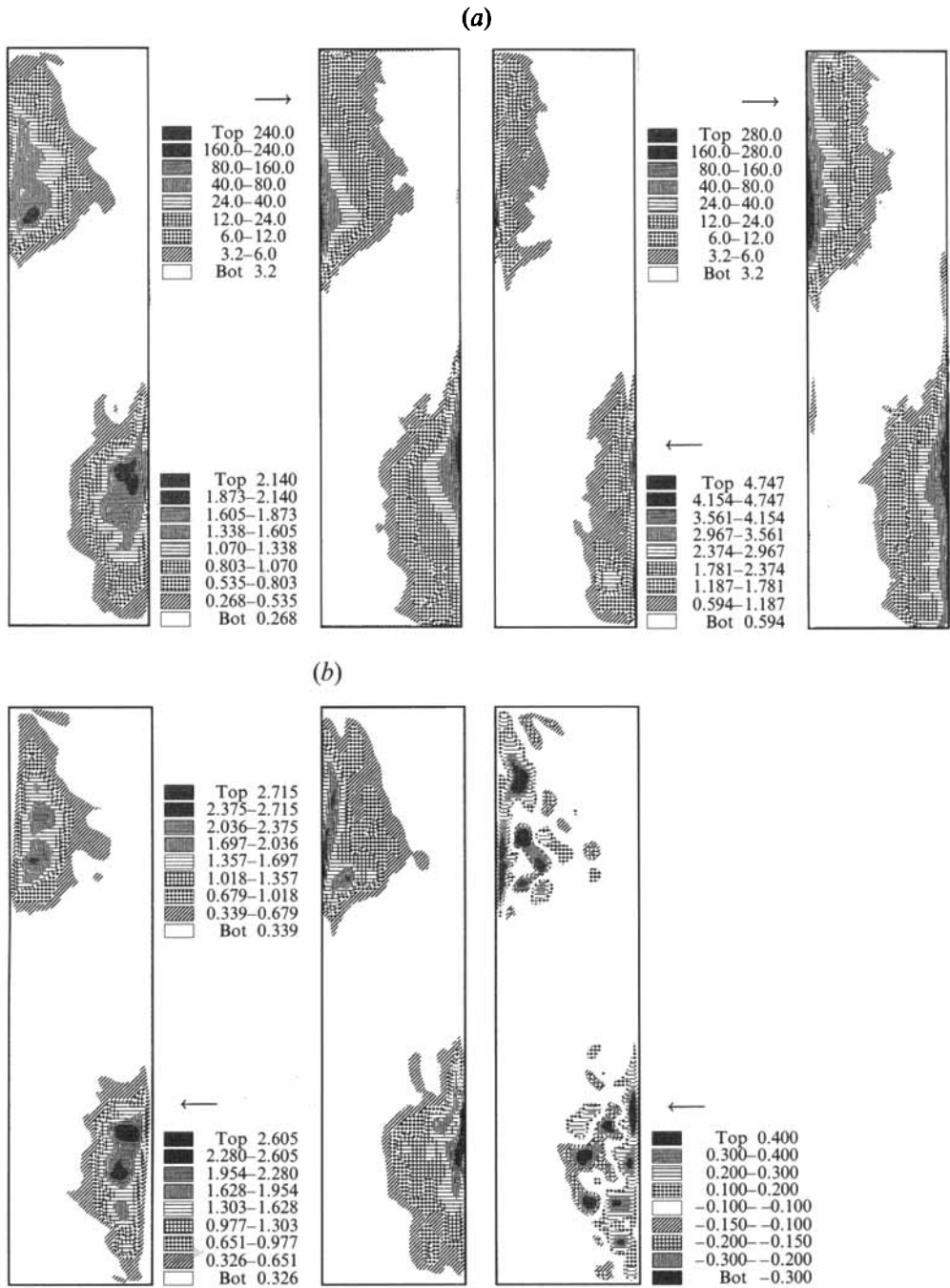
(a)

(b)

FIGURE 15 *(a,b)*. For caption see next page

the time-averaged fields. Assuming v_t and σ_t to be positive, the signs of $\overline{u'w'}$, $\overline{u'\Theta'}$ and $\overline{w'\Theta'}$ should correspond respectively with those of $-(\partial\overline{u}/\partial z + \partial\overline{w}/\partial x)$, $-\partial\overline{\Theta}/\partial x$ and $-\partial\overline{\Theta}/\partial z$. Our results clearly show that this sign match does not seem to hold. Since we have seen that this flow configuration is characterized by the coexistence of 'turbulent' and laminar regions in the cavity and that the second-order statistics
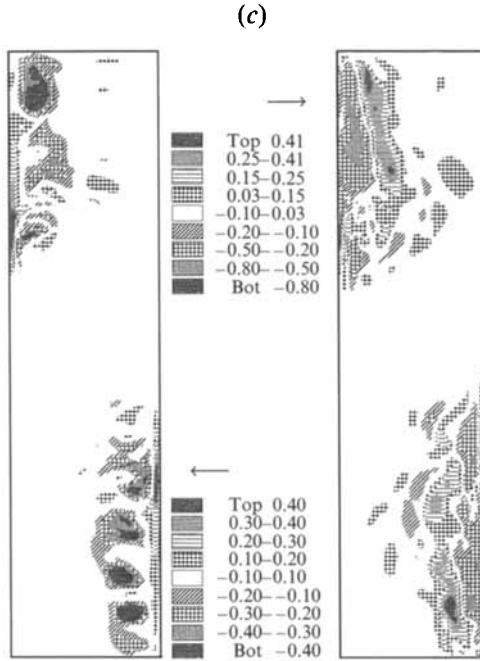
(c)

FIGURE 15. (a) Turbulent statistics at $Ra = 10^{10}$; from left to right: k, ϵ_v, $\overline{\Theta'^2}$ and ϵ_Θ. k and $\overline{\Theta'^2}$ should be multiplied by 10^{-3}. The maximum values for ϵ_v and ϵ_Θ are 1800 and 850. (b) Turbulent statistics at $Ra = 10^{10}$: $\overline{u'^2}$, $\overline{w'^2}$ and $\overline{u'w'}$ (from left to right). The scale of the Reynolds stresses should be multiplied by 10^{-3}. (c) Turbulent statistics at $Ra = 10^{10}$: $\overline{u'\Theta'}$ and $\overline{w'\Theta'}$ (from left to right). The scale of the turbulent heat fluxes should be multiplied by 10^{-3}.

also show that the flow anisotropy is very large, one can conclude that standard k-ϵ modelling is not appropriate for turbulent natural convection flows in cavities. It is thus necessary to take into account low-Reynolds-number effects but since this approach still assumes turbulence to be isotropic, to go further towards second-order Reynolds stress modelling as Ince *et al.* (1992) did.

3.5. *Heat transfer*

For the three Rayleigh numbers considered, time-averaged and spatial mean Nusselt numbers (the reference heat flux is $\lambda \Delta T/H$) are given in table 2. The value obtained at the highest Rayleigh number is in very good agreement with that obtained by Paolucci (1990) and Le Quéré (1994a). This confirms that the aspect ratio has a minor effect on the heat transfer through a cavity with adiabatic horizontal walls. The heat transfer thus seems to depend only on the Rayleigh number based on the cavity height, at least for aspect ratios in the range 1–4. We have listed in columns 3 and 4 of table 2 the proportionality constants for the two classical correlations, $Ra^{1/4}$ for laminar and $Ra^{1/3}$ for turbulent flows. These values show that the Nusselt number follows a correlation between $Ra^{1/4}$ and $Ra^{1/3}$ but the heat transfer correlation is still much closer to $Ra^{1/4}$ than to $Ra^{1/3}$, despite what was, not so long ago, thought of as a very large Rayleigh number. Time-averaged local Nusselt number and its minimum and maximum envelopes in time (figure 16) show that in the upstream part of the boundary layer where the flow is essentially laminar the fluctuations of Nusselt number are very small while in the downstream part of the boundary layer we observe
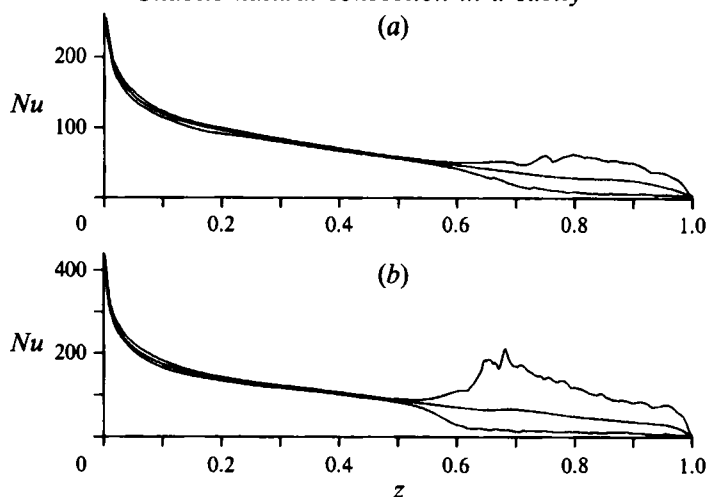
FIGURE 16. Local Nusselt number distributions and their maximum and minimum envelopes in time: $Ra = 2 \times 10^9$ (a) and $Ra = 10^{10}$ (b).

Ra	$\overline{Nu}$	$\overline{Nu}/Ra^{1/4}$	$\overline{Nu}/Ra^{1/3}$
6.4×10^8	49.2	0.309	0.0571
2.0×10^9	66.5	0.315	0.0528
1.0×10^{10}	101.0	0.319	0.0469

TABLE 2. Nusselt number and correlation

very important fluctuations of the local Nusselt number. These large fluctuations are due to the large eddies generated in the downstream part of the boundary which result in alternative local thickening or thinning of the thermal boundary layer. These large eddies also result in an efficient mixing of the outer region of the boundary layer and to enhanced fluid transport from the downstream part to the corresponding facing upstream part of the opposite boundary layer. Figure 16 also shows that the region which sustains large fluctuations of the local Nusselt number increases with Rayleigh number and, at $Ra = 10^{10}$, important fluctuations of Nusselt number are observed just above cavity mid-height. However and rather disappointingly, since most of the heat transfer occurs in the upstream regions, the large fluctuations in the downstream region have little effect on the mean heat transfer coefficient.

4. Conclusions

From the two-dimensional direct simulations which were performed in a cavity of aspect ratio 4 filled with air for Rayleigh numbers up to 10^{10}, the following conclusions can be drawn: for the Rayleigh numbers considered, the vertical boundary layers remain laminar at least over their first half and they then undergo a rapid transition just above mid-height resulting from the strong amplification of Tollmien–Schlichting waves; the isotherms in the boundary layers show hook-like patterns which correspond to large eddies which are ejected into the cavity core; the cavity core remains well stratified in the mean and the stratification remains larger than $\Delta T/H$ at mid-cavity height, especially for the highest Rayleigh number investigated; when the Rayleigh number becomes large enough, internal waves in the core region get permanently

excited and oscillate at the Brunt–Väisälä frequency; even for the largest Rayleigh number investigated, second-order statistics are only significant in the downstream part of the vertical boundary layers; $\overline{u'^2}$ and $\overline{w'^2}$, the kinetic energy k and the turbulent viscous dissipation ϵ_v are not very well spatially correlated, but $\overline{w'^2}$ and $\overline{\Theta'^2}$, the turbulent viscous dissipation ϵ_v and the turbulent thermal dissipation ϵ_Θ do show some spatial coherence; the most important contributions to ϵ_v and ϵ_Θ come from $\partial w'/\partial x$ and $\partial \Theta'/\partial x$ and are found very close to the vertical walls; for Rayleigh numbers up to 10^{10}, the mean Nusselt number still follows a $Ra^{1/4}$ relationship.

The present direct numerical simulations also offer a complete data set of time-averaged fields and second-order statistics such as turbulent Reynolds stress, variances of temperature and velocity components, turbulent kinetic energy, its viscous dissipation rate, thermal dissipation rate and turbulent heat fluxes. They can be used for validating turbulence models developed for weakly turbulent natural convection, both for the time-averaged fields and for the second-order statistics. It was clearly shown that in the range of Rayleigh values investigated laminar and 'turbulent' flows coexist in the cavity and that wall and stratification effects result in large flow anisotropy. Second-moment closure modelling therefore seems the most promising way to obtain realistic and deterministic turbulence models in the present configuration and more generally in turbulent buoyant flows along walls. Also, further investigations are needed to understand the role of the internal waves on the flow dynamics and their implications for turbulence modelling. Owing to the limitations of the present two-dimensional direct numerical simulations, future three-dimensional simulations will show the importance of allowing for extra degrees of freedom in the third direction on the structure of the mean flow and turbulence quantities. Comparisons with solutions obtained with turbulence models will then be more meaningful.

REFERENCES

ABROUS, A. & EMERY, F. 1989 Turbulent free convection in square cavities with mixed boundary conditions. *Nat. Heat Transf. Conf.* ASME-HTD **107**, 117–130.

ALLARD, F. 1992 Effects of thermal boundary conditions on natural convection in thermally driven cavities. *ERCOFTAC-EUROTHERM Workshop, Delft*, pp. 234–256. EETI.

BEHNIA, M. & LE QUÉRÉ, P. 1992 Direct simulation of turbulent convection in a square differentially heated cavity with spectral methods. *4th Intl Fluid Mech. Conf., Alexandria*.

CRAIK, A. D. D. 1985 *Wave Interactions and Fluid Flows.* Cambridge University Press.

FRAIKIN, M. P. PORTIER, J. J. & FRAIKIN, C. J. 1980 Application of a K-ϵ turbulence model to an enclosed buoyancy-driven recirculating flow. *19th ASME-AIChE Heat Nat. Transfer Conf., Orlando, Florida*, 80-HT-68.

FROMM, J. E. 1971 Numerical method for computing nonlinear, time dependent, buoyant circulation of air in rooms. *IBM J. Res. Dev.* **15**, 186–196.

GEORGE, W. K. & CAPP, S. P. 1979 A theory for natural convection turbulent boundary layers next to vertical heated surfaces. *Intl J. Heat Mass Transfer* **22**, 439–485.

GIEL, P. W. & SCHMIDT, F. W. 1990 A comparison of turbulence modeling predictions to experimental measurements for high Rayleigh number natural convection in enclosures. *9th Intl Heat Transfer Conf.*, Paper 2-NC-03, pp. 175–180.

GRÖTZBACH, G. 1982 Direct simulation of laminar and turbulent Bénard convection. *J. Fluid Mech.* **119**, 27–53.

HAIDVOGEL, D. & ZANG, T. 1979 The accurate solution of Poisson's equations by expansion in Chebyshev polynomials. *J. Comput. Phys.* **30**, 167–180.

HALDENWANG, P. 1984 Résolution tridimensionnelle des équations de Navier-Stokes par méthodes spectrales Tchebycheff. Thèse d'Etat, University de Provence.

HALDENWANG, P. 1986 Unsteady numerical simulation by Chebyshev spectral methods of natural convection at high Rayleigh number. *ASME HTD* **60**, 45–51,

HANJALIC, K. 1994 Achievements and limitations in modelling and computation of buoyant turbulent flows and heat transfer, keynote lecture. *10th Intl Heat Transfer Conf.* IChemE Symposium series, vol. 1, pp. 1–18.

HENKES, R. A. W. M. 1990 Turbulent natural convection boundary layers. PhD Thesis, Delft University of Technology.

HUSSAINI, M. Y., SPEZIALE, C. G. & ZANG, T. 1989 *The Potential and Limitations of Direct and large-Eddy Simulations.* Lecture Notes in Physics, vol. 357. Springer.

INCE, N. BETTS, P. & LAUNDER, B. 1992 Low Reynolds number modeling of turbulent buoyant cavity flows. *ERCOFTAC-EUROTHERM Workshop, Delft*, pp. 76–87.

IVEY, N. G. 1984 Experiments on transient natural convection in a cavity. *J. Fluid Mech.* **34**, 389–401.

JONES, P. W. & LAUNDER, B. E. 1972 The prediction of laminarization with a two-equation model of turbulence. *Intl J. Heat Mass Transfer* **15**, 301–314.

JONES, P. W. & LAUNDER, B. E. 1973 The calculation of low-Reynolds-number phenomena with a two-equation model of turbulence. *Intl J. Heat Mass Transfer* **16**, 1119–1130.

KLEISER, L. & SCHUMANN, U. 1980 Treatment of incompressibility and boundary conditions in three-dimensional numerical spectral simulations of plane channel flows. *Notes on Numerical Fluid Mechanics*, Vol. 2, pp. 165–173.

LE BRETON, P. 1991 Etude numérique et expérimentale de la convection naturelle laminaire et turbulente en cavité partiellement occupée d'un milieu poreux. Thèse de Doctorat, University of Bordeaux.

LE QUÉRÉ, P. 1987 Etude de la transition à l'instationnarité des écoulements de la convection naturelle en cavité verticale différentiellement chauffée par méthodes spectrales Chebyshev. Thèse d'Etat, University of Poitiers.

LE QUÉRÉ, P. 1991 Accurate solutions to the square thermally driven cavity. *Computers Fluids* **20**, 29–41.

LE QUÉRÉ, P. 1994a An improved Chebyshev collocation algorithm for direct simulation of two-dimensional turbulent convection in differentially heated cavities. *Finite Elements Anal. Design* **16**, 271–283.

LE QUÉRÉ, P. 1994b Onset of unsteadiness, routes to chaos and simulations of chaotic flows in cavities heated from the side : a review of present status, keynote lecture. *10th Intl Heat Trans. Conf.* IChemE Symposium Series, vol. 1, pp. 281–296.

LE QUÉRÉ, P. & ALZIARY DE ROQUEFORT, T. 1982 Sur une méthode spectrale semi-implicite pour la résolution des équations de Navier-Stokes d'un écoulement bidimensionnel visqueux incompressible. *C. R. Acad. Sci. Paris* **294**(II), 941–944.

LE QUÉRÉ, P. & ALZIARY DE ROQUEFORT, T. 1985 Computation of natural convection in two-dimensional cavities with Chebyshev polynomials. *J. Comput. Phys.* **57**, 210–228.

LE QUÉRÉ, P. & BEHNIA, M. 1994 From onset of unsteadiness to chaos in a differentially heated square cavity. *LIMSI Rep.* 94–02. (also submitted to *J. Fluid Mech.*).

LE QUÉRÉ, P. & PENOT, F. 1987 Numerical and experimental investigation of the transition to unsteady natural convection of air in a vertical differentially heated cavity. *ASME HTD* **94**, 75–82.

LIGHTHILL, J. 1978 *Waves in Fluids* Cambridge University Press.

LIPPS, F. 1976 Numerical simulation of three-dimensional Bénard convection in air. *J. Fluid Mech.* **75**, 113–148.

MARKATOS, N. C. & PERICLEOUS, K. A. 1984 Laminar and turbulent natural convection in an enclosed cavity. *Intl J. heat Mass Transfer* **27**, 755–772.

MERGUI, S., PENOT, F. & TUHAULT J. L. 1992 Experimental natural convection in an air-filled square cavity at $Ra = 1.7 \times 10^9$. *ERCOFTAC-EUROTHERM Workshop, Delft*, pp. 97–108, EETI.

NDAME, A. 1992 Etude expérimentale de la convection naturelle en cavité: de l'état stationnaire au chaos. Thèse de Doctorat, University of Poitiers.

NOBILE, E., SOUSA, A. C. M. & BAROZZI, G. S. 1990 Turbulent buoyant flows in enclosures. *9th Intl Heat Transfer Conf.*, Paper 5-NC-11, pp. 543–548.

OZOE, H., MOURI, A., HIRAMITSU, M., CHURCHILL, S. W. & LIOR, N. 1986 Numerical calculation of three-dimensional turbulent natural convection in a cubical enclosure using a two-equation model for turbulence. *J. Heat Transfer* **108**, 806–813.

PAOLUCCI, S. 1990 Direct simulation of two-dimensional turbulent natural convection in an enclosed cavity. *J. Fluid Mech.* **215**, 229–262.

PAOLUCCI, S. & CHENOWETH, D. R. 1989 Transition to chaos in a differentially heated vertical cavity. *J. Fluid Mech.* **201**, 379–410.

PATTERSON, J. & ARMFIELD S. W. 1990 Transient features of natural convection in a cavity. *J. Fluid Mech.* **219**, 469–497.

PATTERSON, J. & IMBERGER, J. 1980 Unsteady natural convection in a rectangular cavity. *J. Fluid Mech.* **100**, 65–86.

PENOT, F., NDAME, A. & LE QUÉRÉ, P. 1990 Investigation of the route to turbulence in a vertical differentially heated cavity *9th Intl Heat Transfer Conf.* vol. 2, pp. 417–422.

STEINBERNER, U. & RAINEKE, H. H. 1978 Turbulent buoyancy convection heat transfer with internal heat sources. *6th Intl Heat Transfer Conf.* vol. 2, pp. 305–310.

STUHMILLER, J. H. 1979 Theoretical considerations of turbulent buoyant flows. *Heat Transfer and Turb. Buoy. Convection*, vol. 1, pp. 3–14.

TO, W. M. & HUMPHREY, J. A. C. 1986 Numerical simulation of buoyant turbulent flow–I and II. *Intl J. Heat Mass Transfer* **29**, 573–610.

TUCKERMAN, L. 1989 Divergence-free velocity field in non-periodic geometries. *J. Comput. Phys.* **80**, 403–441.

UITENBORGAARD, R. E. & BARON, F. 1989 A proposal: extension of the $q^2 - \epsilon$ model for stably stratified flows with transport of internal wave energy. *7th Turbulent Shear Flows Conf, Stanford, USA.*

VAHL DAVIS, G. DE & JONES, I. P. 1983 Natural convection in a square cavity: a comparison exercise. *Intl J. Numer. Meth. Fluids* **3**, 227–248.

VANEL, J. M., PEYRET, R. & BONTOUX, P. 1986 A pseudo-spectral solution of vorticity–streamfunction equations using the influence matrix technique. *Num. Meth. Fluid Dyn.* **2**, 463–475.

XIN, S. 1993 Simulations numériques de convection naturelle turbulente, Thèse de Doctorat, University of Paris VI.

XIN, S. & LE QUÉRÉ, P. 1992 Direct simulation of turbulent natural convection in a differentially heated cavity of aspect ratio 4 with spectral methods. *1st Eur. Thermal Sciences Conf., Birmingham*, vol. 1, pp. 475–482.

XIN, S. & LE QUÉRÉ, P. 1994 Numerical simulations of two-dimensional turbulent natural convection in differentially heated cavities of aspect ratios 1 and 4. *1st EUROTHERM ERCOFTAC Workshop on Direct and Large Eddy Simulation, University of Surrey*, pp. 423–434.